Simulation of the eThekwini Heat Island in South Africa

ROBERT T. MAISHA,[a,b] THANDO NDARANA,[b] FRANCOIS A. ENGELBRECHT,[c] MARCUS THATCHER,[d] MARY-JANE M. BOPAPE,[b,e] JACOBUS VAN DER MERWE,[f] YERDASHIN PADAYACHI,[f] AND CECILIA MASEMOLA[f]

[a] *Weather Research, South African Weather Service, Pretoria, South Africa*
[b] *Department of Geography, Geoinformatics and Meteorology, University of Pretoria, Pretoria, South Africa*
[c] *Global Change Institute, University of the Witwatersrand, Johannesburg, South Africa*
[d] *Commonwealth Scientific and Industrial Research Organisation, Aspendale, Victoria, Australia*
[e] *South African Earth Observations Network, National Research Foundation, Pretoria, South Africa*
[f] *Smart Places, Council for Scientific and Industrial Research, Pretoria, South Africa*

(Manuscript received 26 November 2021, in final form 22 March 2023, accepted 27 March 2023)

ABSTRACT: The study evaluates the performance of the Conformal Cubic Atmospheric Model (CCAM) when simulating an urban heat island (UHI) over the city of eThekwini, located along the southeast coast of South Africa. The CCAM is applied at a grid length of 1 km on the panel with eThekwini, in a stretched-grid mode. The CCAM is coupled to the urban climate model called the Australian Town Energy Budget (ATEB). The ATEB incorporates measured urban parameters including building characteristics, emissions, and albedo. The ATEB incorporates the land-cover boundary conditions obtained from the Moderate Resolution Imaging Spectroradiometer (MODIS) satellite. The CCAM configuration applied realistically captured the orientation of the city and land-cover types. Simulations of meteorological variables such as temperatures and longwave radiation reproduced the spatial distribution and intensity of the UHI. Results show that the UHI is stronger during summer and weaker in all other seasons. The UHI developed because of natural factors (e.g., distribution of longwave radiation) and human factors (e.g., urban expansion, an increase in anthropogenic emissions, and additional heating). Because of the city's location along the coast, the UHI simulation could be weakened by atmospheric circulations resulting from land and sea breezes. Mitigation methods such as applying reflective paints and revegetation of the city may increase albedo and latent heat fluxes but reduce the sensible heat fluxes and weaken the UHI. However, the UHI may not be completely eliminated since natural factors and emissions constantly influence its development.

SIGNIFICANCE STATEMENT: The outcome of this study could be particularly valuable for municipalities in their disaster management planning since the occurrence of UHIs can cause heat-related diseases such as heatstrokes and even fatalities, especially for the elderly, in cities. Increases in temperatures also lead to higher demand for air conditioners, which in the long term lead to higher demand and pressure on the electricity grid system as well as increased costs for the individual. As higher temperatures increase heatwave events, increases in anthropogenic emissions also result in degraded air quality that impacts health. UHIs impact human lives and can cause deterioration in health when individuals experience high temperatures in summer. Warmer temperatures also reduce energy demand (and in the long term assist with global environmental restoration).

KEYWORDS: Atmosphere; Africa; Indian Ocean; Atmosphere–land interaction; Land surface model

1. Introduction

Currently, more than 50% of the world's population lives in cities (Oleson et al. 2011; Pokhrel and Lee 2011; Han et al. 2014; Heaviside et al. 2017; Zhang et al. 2022; Barrao et al. 2022). Because of increasing urbanization, this number is projected to increase to more than 60% by the mid-twenty-first century (Walsh et al. 2013; Garuma 2018). Growth in urbanization has resulted in increases in infrastructure requirements in cities, including transportation, water, and power supply (Baklanov et al. 2018; Garuma 2018). The development that is associated with urbanization leads to the modification of surfaces from natural to artificial, such as concrete and asphalt surfaces (Ramamurthy et al. 2014), and increased requirements for heating. While this may represent progress, one of its consequences is that vegetation cover in cities has been reduced. This has also resulted in increased anthropogenic emissions of greenhouse gases and modified radiative forcing. Urbanization contributes to global warming and may influence climate change and result in the development of urban heat islands (UHIs; Nuruzzaman 2015; Lehoczky et al. 2017; Chapman et al. 2019). Thus, urban growth causes an increase in nighttime temperatures, which results in the development of UHIs (Karl et al. 1993; Hughes and Balling 1996; Sharma et al. 2016; Wang and Li 2017; Grimmond et al. 2011; Bohnenstengel et al. 2011; Lemonsu et al. 2023).

Artificial surfaces found in urban areas absorb shortwave radiation and radiate longwave at the end of the electromagnetic spectrum. This is attributed to the materials' storage heat flux density, which is the net flow of heat per unit area, into or out of the material (Lipson et al. 2017). The situation is reversed in rural areas where higher vegetation constitutes a higher albedo, and a larger portion of the incoming shortwave radiation is reflected. Consequently, the heat stored in rural areas during the day is less than the heat stored in urban

Corresponding author: Robert T. Maisha, robert.maisha@weathersa.co.za and trmaisha@gmail.com

DOI: 10.1175/JAMC-D-21-0231.1

areas (Baklanov et al. 2018; Garuma 2018; Lehoczky et al. 2017), and thus, rural areas do not radiate as much longwave radiation as the urban areas. Since increases in atmospheric temperatures are caused by the absorption of longwave radiation, cities become warmer by an average of 2°C (Chapman et al. 2019) than the surrounding rural areas, creating the UHI (Baklanov et al. 2018; Garuma 2018; Lehoczky et al. 2017; Luhar et al. 2014; Walsh et al. 2013; Taha 1997; Nuruzzaman 2015; Bohnenstengel et al. 2011). When temperature difference between urban and rural areas during nighttime is highest, this metric is used as a measure of UHI intensity (Heaviside et al. 2017; Zhang et al. 2022).

Wilby (2008) studied UHI intensity and air quality over the city of London. The UHI intensity was defined as the daily minimum temperature difference between a station within the city and in a rural area. An intense nocturnal UHI was defined as occurring when the temperature difference between rural and urban exceeds 4°C. The UHI was also found to be higher under clear sky conditions, low humidity, and low wind speed (Wilby 2008; Heaviside et al. 2017; Zhang et al. 2022). Heaviside et al. (2017) studied/reviewed the UHI over the city of London and its impacts on health during heatwaves. During an intense/extreme UHI, nighttime temperature difference between urban and rural areas was found to be 5°–10°C in larger cities, in agreement with Bohnenstengel et al. (2011), Heaviside et al. (2017), and Barrao et al. (2022).

Zhang et al. (2022) studied the UHI intensity over the mountainous city of Chongqing, China, with a focus on the temperature difference between rural and urban stations. The study found greater nighttime warming in urban than in rural areas, resulting in an average UHI intensity of 1.5°C for the mountainous city of Chongqing after 2015. The study found that urbanization has a statistically significant influence on daily minimum temperatures. The positive temperature trend is found to be higher during spring and summer months over urban areas. Coutts et al. (2007) studied the UHI over the city of Melbourne, Australia, using different urban density levels, namely, the central business district and high-, medium-, and low-density as well as rural areas. The study found a large difference in the latent heat flux between rural and urban areas due to more vegetation cover and water storage in rural areas.

Lemonsu et al. (2023) studied the urban climate over Paris, France, using a high-resolution CNRM-AROME model at a resolution of 2.5 km driven by European Centre for Medium-Range Weather Forecasts (ECMWF) interim reanalysis (ERA-Interim) data. The study showed that a higher-resolution model captures urban-scale events such as the UHI very well. The study also confirms that high-resolution climate models that incorporate specific urban surface processes could be used to diagnose climate and its impacts at city scale and their evolution in a changing climate. Urban heating leads to cities becoming more vulnerable to extreme weather (Schleussner et al. 2016) and climate change impacts (Chen et al. 2014; Mirzaei 2015; Garuma 2018; Chapman et al. 2019; Lipson et al. 2018). The UHI is exacerbated by air pollutants from industries, power generation, air conditioners, and exhaust gases since they increase anthropogenic heating (Yang et al. 2013; Nuruzzaman 2015; Zhang et al. 2022). The UHI results in compromised health (Zhang et al. 2022; Barrao et al. 2022) of the urban population, through exposure to higher temperatures during heatwaves, leading to respiratory illness, hospitalization, and death (Heaviside et al. 2017). Heatwaves also intensify the temperature difference between rural and urban areas during UHIs (Barrao et al. 2022).

Although UHI intensity and magnitude impact cities and have been studied in other global cities, they have not been modeled over South African cities. Therefore, it is important to study UHIs and the different mechanisms responsible for their formation using both observations and high-resolution atmospheric models set up with urban-scale features (Wang and Li 2017; Garuma 2018). Urban climate models (UCMs) are coupled to regional atmospheric models to investigate the dynamics of the urban climate resulting from global emission scenarios and could be used for urban planning (Thatcher and Hurley 2012). Initially, UCMs were developed from slab models with urban settings viewed as a concrete plate composed of a modified roughness length and thermal properties (Luhar et al. 2014) suitable for simulating urban energy budget (Thatcher and Hurley 2012). With advances in technology and innovation, UCMs were further developed, taking into account the energy budget from roofs, roads, and walls (Luhar et al. 2014; Masson 2000). Currently, these models are built in a manner that incorporates all the urban physical parameters such as heat fluxes, radiation, and anthropogenic emissions, as also done in the model applied in this study, the Australian Town Energy Budget (ATEB; Masson 2000; Thatcher and Hurley 2012; Luhar et al. 2014; Garuma 2018).

The UHI existence has been inferred indirectly from observed temperature trends in South Africa. Specifically, observation studies show that temperatures have increased in South African cities more rapidly than in rural areas due to the UHI effect (Kruger and Shongwe 2004). They found a statistically significant warming trend of minimum temperatures by 0.34°C decade^{-1} over urban stations. Historical simulations of surface temperatures for the period 1951–2005 with a regional climate model by Kruger et al. (2019) underestimated observed annual average minimum temperatures by at least 0.05°C decade^{-1}.

Globally, UHI simulations with UCMs were performed in various cities. Bozonnet et al. (2007) modeled winds and natural convection flows over the urban street in Athens. The study found that when winds interact with local topography, they trigger either land or seas breezes. This causes temperature variations on both micro- and urban scales, which move from surroundings to cities, thus causing warm air to rise in the city due to the UHI. The UHI effect reaches its maximum at night when wind velocity is low (Bozonnet et al. 2007), and the UHI gets dispersed during windy days. In buildings with air conditioners and condensers mounted on exterior walls, the condenser produces heat and increases the UHI within the canyons/streets (Bozonnet et al. 2007; Thatcher and Hurley 2012). Lipson et al. (2017) applied the ATEB to study heat conduction through urban materials. The storage heat flux density of urban materials was found to affect environmental stability, boundary layer profile, convection, and the UHI. Lipson et al. (2018) developed an integrated building energy demand and urban land surface model called the Urban

Climate and Energy Model (UCLEM) to improve the predictability of building energy demand and to study the different impacts of urban planning decisions on current and future climates.

In this study, we apply the Conformal Cubic Atmospheric Model (CCAM) coupled to the ATEB. This model works as both a global model and a regional climate model in stretched-grid mode. The CCAM has been applied in many regional climate studies such as Sri Lanka (Thevakaran et al. 2016), Vietnam (Nguyen et al. 2014), and South Africa (Engelbrecht et al. 2009, 2011, 2015; Garland et al. 2015; Muthige et al. 2018; Engelbrecht et al. 2019).

The ATEB was developed as an urban component of a global climate model, which takes into consideration building and street characteristics (Lipson et al. 2017). It was conceptualized from the Town Energy Budget (TEB) model developed by Masson (2000), but with some customizations for Australia (Lipson et al. 2017). The ATEB is a microscale model used to investigate the energy budget within an urban canopy layer (Mirzaei 2015). In addition to the ability to resolve heat transfer, the ATEB includes a planetary boundary layer turbulence closure parameterization (Chen et al. 2015; Thatcher and Hurley 2012). Because of its spatial scale, the ATEB can simulate the urban canopy and separate different energy budgets (Ramamurthy et al. 2014; Garuma 2018) and is able to simulate urban features (Han et al. 2014) such as the UHI (Chen et al. 2011; Garuma 2018). The ATEB also considers temperature diurnal variation within the canyon by including the west- and east-facing walls. The ATEB also incorporates a big-leaf model, which represents in-canyon vegetation as well as the parameterization of air conditioners to cater for the energy conservation (Lipson et al. 2017; Luhar et al. 2014; Thatcher and Hurley 2012). The urban parameters are applied to refine the urban surfaces within the UCMs (Garuma 2018) and also influence heat removal from surfaces of buildings (Mirzaei 2015). Similar types of experiments with ATEB settings were performed by Luhar et al. (2014) over the city of Basel, Switzerland, and also in Brisbane, Australia (Chapman et al. 2019). Some further developments of the ATEB are described in Lipson et al. (2018).

In this study, we interrogate these questions: 1) Does the UHI exist over the city of eThekwini? 2) If so, can a climate model simulate a UHI? 3) How can the improvement of land-cover and measured urban parameters improve the simulation of the UHI? This study is the first application of a dynamical study of the UHI over a coastal city of South Africa. The UCM simulation is performed at a high resolution of 1 km and is coupled to a regional climate model, the CCAM as described in Taha (1997) and Thatcher and Hurley (2012).

The study applies the model at high resolution with the expectation that ingesting the land use at high resolution will result in the model capturing the UHI impacts well to inform adaptation and mitigation strategies. The rest of the paper is outlined as follows: in section 2, the data, model setup, and methods applied are discussed; section 3 focuses on the results; section 4 presents the discussion; and section 5 presents the summary and draws conclusions from the study.

2. Methods

a. Study area

The CCAM is applied at a resolution of 1 km over the eThekwini metropolitan municipality. The city is located along the southeast coast of the KwaZulu-Natal province of South Africa with its center at 29.86°S and 31.02°E. The city is highly urbanized, especially along the coastline, as depicted in the land-cover classification (Fig. 1). The city is classified as a summer rainfall region (Cook et al. 2004). The area experiences a warm, fully humid, and hot summer climate (Cfa; Kottek et al. 2006; Engelbrecht and Engelbrecht 2016), with a minimum temperature higher than +18°C (Kottek et al. 2006). Observation studies (e.g., Kruger and Shongwe 2004) over the area (Durban weather station) indicate a significant increase in hot nights, with a warming trend of 0.1°C decade^{-1} for maximum temperature and 0.346°C decade^{-1} for minimum temperature, and this was attributed to urbanization (Hughes and Balling 1996).

For the historical period 1951–2005, observation and multimodel mean diurnal temperature ranges show nighttime warming over coastal areas, with a decrease in the number of cold nights in the range of less than −2.5% decade^{-1}, which contributed to an increase in daytime warming (Kruger et al. 2019). Future projections (2025–95) indicate a warming trend with both representative concentration pathway 4.5 (RCP4.5) and RCP8.5, but with stronger and more significant warming with RCP8.5, with the number of days increasing by +2.5% decade^{-1}, including coastal stations (Kruger et al. 2019).

b. The model

The CCAM was developed at the Commonwealth Scientific and Industrial Research Organisation (CSIRO) by McGregor (1996). It is both a variable and quasi-uniform resolution model that numerically solves a set of quasi-elastic equations in a terrain-following coordinate system (Engelbrecht et al. 2007) using a semi-implicit, semi-Lagrangian scheme (McGregor 1996). The CCAM may be applied seamlessly across different spatial and time scales, for both weather and climate simulations (Engelbrecht et al. 2011; Thevakaran et al. 2016; Chapman et al. 2019). In stretched-grid mode, the model is able to produce high-resolution simulations over the areas of interest. The CCAM applies a CSIRO9 mass flux scheme based on the Arakawa mass flux scheme (Arakawa 2004). The model also applies a single-moment cloud microphysics scheme based on Rotstayn (1997). The CCAM applies the radiation scheme based on the Geophysical Fluid Dynamics Laboratory Climate Model, version 3 (GFDL CM3; Freidenreich and Ramaswamy 1999). The model applies the turbulent mixing scheme represented by the turbulent kinetic energy as in Hurley (2007). The CCAM is coupled to a dynamic land surface model called CSIRO Atmosphere Biosphere Land Exchange (CABLE), which provides the boundary conditions to the CCAM (Kowalczyk et al. 1994). The CCAM-CABLE incorporates the urban climate model called the ATEB model developed by Thatcher and Hurley (2012), and thus incorporates urban climate processes.

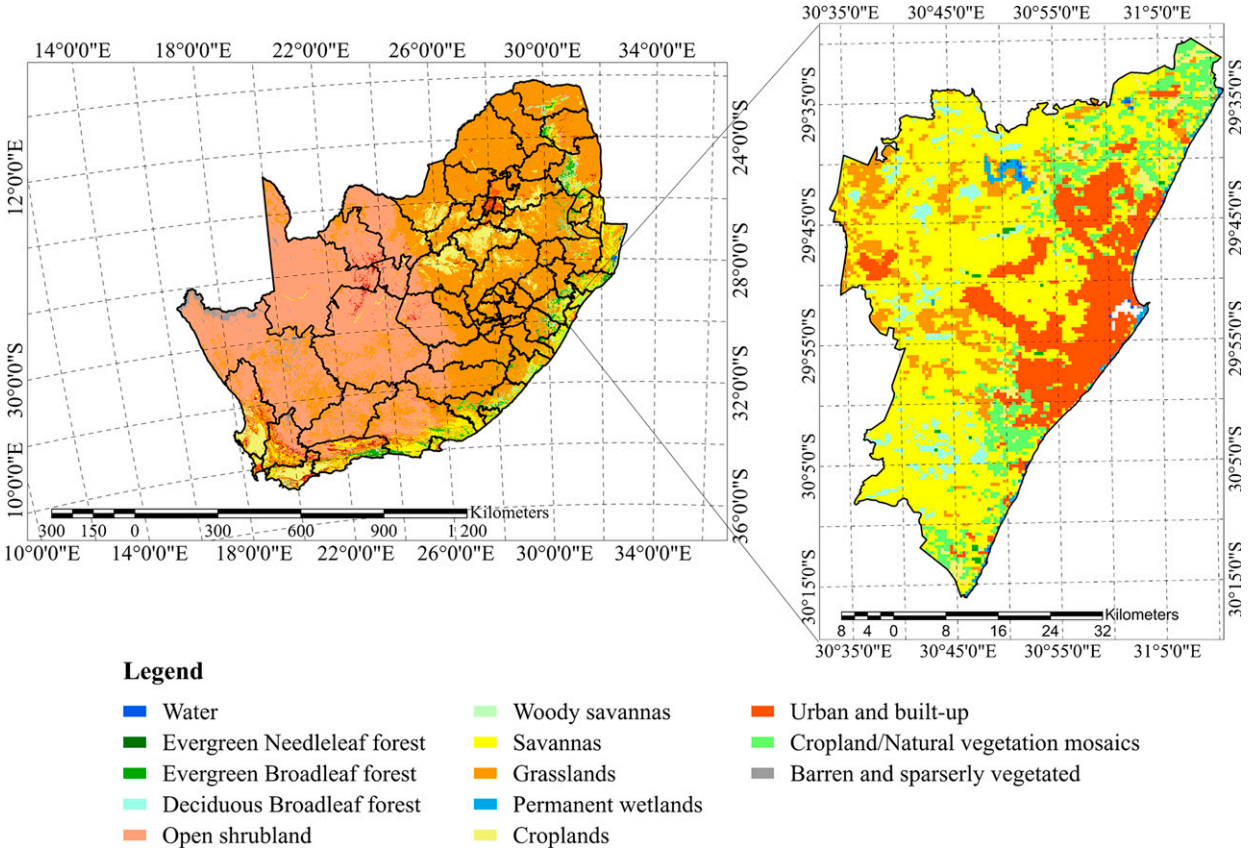

FIG. 1. (left) Map of South Africa and (right) a zoom-in showing the city of eThekwini municipality over the east coast of Kwazulu-Natal, with the MODIS satellite land cover for the period 2013. The urban and built-up areas are depicted in light red along the coastline.

c. *Data collection method*

1) INITIAL AND BOUNDARY CONDITIONS

For this study, a hierarchy of model configurations was developed, with various datasets used. This includes grid lengths of 50, 8, and 1 km applied respectively as follows:

At a global configuration of 50-km resolution, the CCAM is run with initial and boundary conditions obtained from the ERA-Interim data (Dee et al. 2011). The dataset has a horizontal resolution of 0.75° × 0.75° and a temporal resolution of 6 hours (Jones et al. 2017) and is valid for the period 1979–2018; however, for this study, the model is run for the period December 2005–December 2016. The CCAM is forced at its lower boundary with the ERA-Interim sea surface temperatures (SSTs) and sea ice fields (McGregor et al. 2008; Engelbrecht et al. 2009; Dee et al. 2011), while its atmospheric fields were spectrally nudged within the ERA-Interim (Thatcher and McGregor 2009). For this run, the CCAM is coupled to the CCAM-CABLE at a resolution of 50 km to produce static data such as bathymetry, topography, vegetation, and carbon cycle fields.

At 8 km, the CCAM is initialized with the 50-km global output. For this configuration, the CCAM-CABLE applies lower boundary conditions as in the 50-km setting but including the updated land-cover data from the high-resolution Moderate Resolution Imaging Spectroradiometer (MODIS) satellite (https://terra.nasa.gov/about/terra-instruments/modis), which covers South Africa, for the period January–December 2013 (Fig. 1). The MODIS data were mapped to the International Geosphere–Biosphere Programme (IGBP) type 1 description of land cover used by the CCAM-CABLE system. The MODIS data have a horizontal grid spacing of 300 m.

At 1 km, the CCAM is initialized with the 8-km global output. For this configuration, the CCAM-CABLE also applies MODIS-updated land cover for lower boundary conditions, with measured urban parameters from the city added, as it defines the class of the city (i.e., low, middle, high, etc.). However, a generic class has been selected and applied (Table 1).

2) MODEL VALIDATION DATA

For model validation, the model output is validated against two datasets. The first dataset is observations from the South African Weather Service (SAWS) Durban (eThekwini) and Mount Edgecombe automatic weather stations. The Durban station is located at 29.965°S, 30.946°E, at an elevation of approximately 1.2 m above the ground and has an altitude of 14 m above mean sea level (MSL). The model height in meters shows

TABLE 1. The city of eThekwini measured urban (generic) parameters (ATEB-3) and default CCAM parameters (ATEB-1) as well as their differences.

Units	ATEB-3 (measured)	ATEB-1 (default)	Difference
Building heights (m)	5.86	6.00	−0.14
Height to width	0.24	0.40	−0.16
Vegetation fraction (%)	0.25	0.38	−0.13
Building fraction (%)	0.55	0.45	0.10
Industrial emissions (W m^{-2})	1.00	0.00	1.00
Traffic emissions (W m^{-2})	2.62	1.50	1.12
Roof albedo	0.20	0.20	0.00
Wall albedo	0.30	0.30	0.00
Road albedo	0.10	0.10	0.00
Vegetation albedo	0.20	0.20	0.00

the value of 13.99 m, which agrees with the observed station height. Mount Edgecombe station is located at 29.706°S, 31.046°E, approximately 1.2 m above the ground at an altitude of 94 m MSL. The model height in meters shows the value of 101.183 m, which is approximately 7 m higher than the observed level. The dataset includes hourly air temperatures and daily minimum and maximum temperatures for the period December 2005–December 2016. The data are available at 5-min intervals. The acquired raw temperature data comprise the daily hourly, 24-h maximum, and 24-h minimum temperatures from 0100 to 0000 next day and have been averaged at a monthly interval. The data were quality controlled, and missing data were not filled. Because of the longitudinal location of the study area, all of the results are carried out at UTC +2 h, which is South African standard time.

A second dataset, MODIS satellite nighttime land surface temperature (MOD11A1.006) data with a horizontal grid resolution of 1 km, is also used in the study. The dataset is created using a subset of the MOD11A1 products that were downloaded from the Google Earth Engine over the city of eThekwini. The surface temperature distribution has an accuracy of approximately 1 K. Before downloading the data, a bitmask was applied, using the Google Earth Engine platform's JavaScript application programming interface, to ensure that the images are not contaminated by cloud cover. This study only applied imagery with a high-quality flag (QA). The MODIS data were averaged for each of the four seasons for the period December 2012–December 2013.

d. Research process

The current CCAM experiment set up over eThekwini is required to simulate complex coupled processes due to the influence of both sea and atmospheric processes and feedbacks, as well as land cover and topographic features, including UHI effects (Yan et al. 2013). For this study, a hierarchy of model configurations was developed.

First, the CCAM was applied at a quasi-uniform resolution of about 50 km to obtain a simulation of present-day climate, following the experimental design of Horowitz et al. (2017). The CCAM-CABLE, which is coupled to the CCAM, is set up at a resolution of 50 km with a C192 (192 × 192 grid points per panel) centered over Africa (0°, −25°E), and a Schmidt stretch factor of 0.9523 was applied. The CCAM-CABLE produced static data such as bathymetry, topography, vegetation, and carbon cycle fields. The CCAM simulation was performed and produced output at 6-hourly intervals as in section 2c(1)(i) above.

In the second step, the CCAM-CABLE was set up at 8 km over South Africa with updated land cover as described in section 2c(1)(ii) above. The use of updated land cover was motivated by the initial test study with default land cover that displayed no dynamical changes in vegetation fraction and no changes in UHI throughout the various seasons. The CCAM-CABLE was set up at a resolution of 8 km with a C192 (192 × 192 grid points centered per panel) centered over southern Africa (−28°S, 25°E) and a Schmidt stretch factor of 0.1523. This high-resolution panel spans an area of about 1536 km × 1536 km over southern Africa, with a resolution gradually decreasing outside this region. The CCAM output at 50-km resolution global simulations were subsequently used to provide the initial conditions for 8-km simulations, and simulation produced output every 6 h.

Third, for the urban-scale modeling at 1 km, the CCAM-CABLE lower boundary conditions were updated using a high-resolution MODIS land cover as in the 8-km setup. The CCAM-CABLE was also updated with measured urban parameters and emissions from the city of eThekwini shown in Table 1. See also, for example, Luhar et al. (2014) and Chapman et al. (2019) for similar settings. The CCAM-CABLE was set up with a C192 (192 × 192 grid points centered per panel) centered at (30°S, 30°E) with a Schmidt stretch factor of 0.019.

Stretching the grid instead of nesting the higher-resolution model within a coarser resolution helps with avoiding well-known nesting problems such as reflections of atmospheric waves at the lateral boundaries (Engelbrecht et al. 2009). The CCAM 8-km output at six hourly intervals was used to provide initial conditions for an ultrahigh-resolution urban-scale simulation.

Measured urban parameters selected are representative of the entire urban area by averaging over factors such as heights and widths of buildings as well as roads. In Garuma (2018), similar types of setups were described, but with 10 different urban classes. At this resolution, the model applied an integration time step of 18 s, with 27 vertical levels. In addition, the model applied sigma coordinates with levels from 0.9978 up to 0.004 458 01 hPa, and the hourly output was produced to study the UHI over eThekwini.

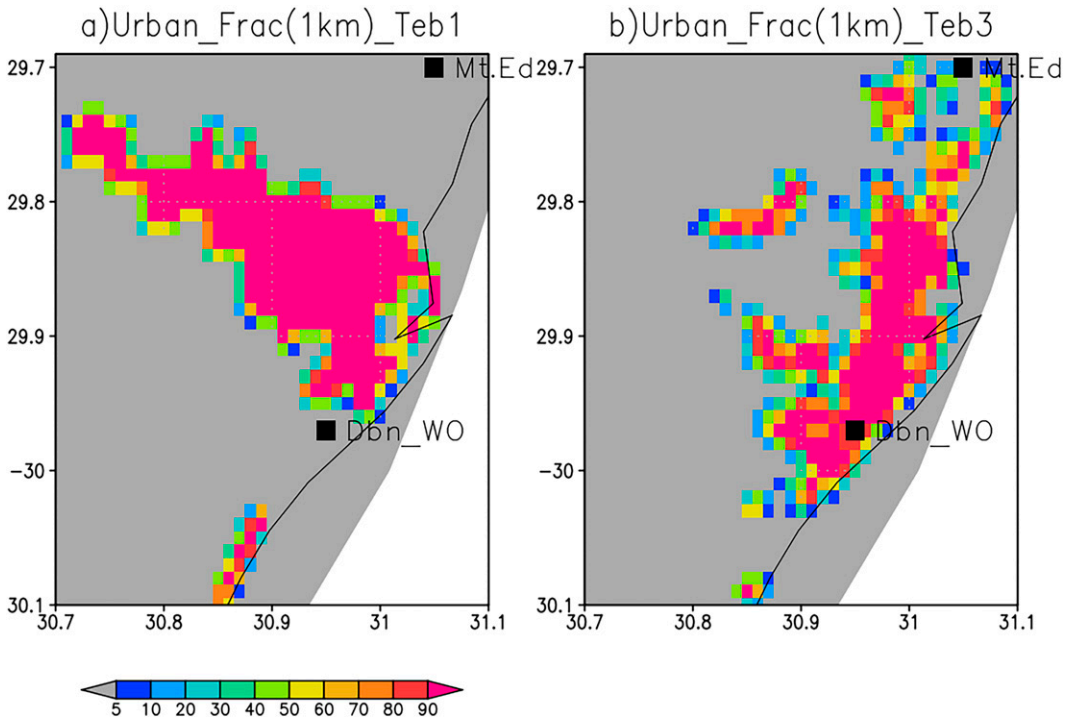

FIG. 2. The CCAM 1-km representation of urban fraction for simulation with both the (a) default and (b) updated land cover over the city of eThekwini.

e. CCAM validation

For the CCAM validation, the station observation dataset described in section 2c(2) (i) is used. Daily hourly averages were calculated over different seasons—that is, summer [December, January, and February (DJF)], autumn [March, April, and May (MAM)], winter [June, July, and August (JJA)], and spring [September, October, and November (SON)]—using both simulations and observation datasets. The average diurnal cycle was also calculated using both datasets. The monthly average error was also calculated between observations and simulated temperatures. The bias and root-mean-square error (RMSE) are also calculated with reference to Gordon and Shaykewich (2000) for the four seasons separately as well as for the whole year.

The CCAM was also validated against MOD11A1.006 satellite nighttime land surface temperature as described in section 2c(2)(ii). The CCAM output was regridded to the MODIS grid of 1 km, and spatial correlation coefficients were calculated for the four seasons. The extracted temperature data have a similar acquisition period as the MODIS land-cover data (Fig. 1).

3. Results

a. Surface representation over eThekwini

Results presented here are for the urban climate simulations over the city of eThekwini at a horizontal grid spacing of 1 km with updated land-cover and measured urban parameters. Figure 2 depicts the default finer resolution (Fig. 2a) and updated urban fraction (Fig. 2b). The updated representation of the surface is more realistic because the simulation is able to identify the correct orientation and spatial distribution of the city as shown in the land-cover map (Fig. 1) and the urban fraction (Fig. 2b). The model setup with the default land-cover data shows higher values of urban fraction spatially distributed in a southeast to a northwest direction (Fig. 2a). However, in the simulation with updated land cover, the highly urbanized area has a southwest to northeast orientation, with more than 90% urbanized areas located along the coastline. According to Lemonsu et al. (2023), such an area is considered to be dense urban. This area spans about 30°–29.8°S = 0.2° or ~20 km from north to south and about 30.85°–31.05°E = 0.2° or ~20 km west to east as in Fig. 2b. The model is able to capture the dynamic monthly and seasonal variability of vegetation cover (not shown).

b. Comparison between observed and model simulations

1) COMPARISON WITH WEATHER STATION DATA FOR THE PERIOD 2006–16

The study applies data from the two available stations over the city of eThekwini from the SAWS network, namely, Durban weather office and Mount Edgecombe; their location is shown in Fig. 2. These observation data were compared with the CCAM simulations. Model data were interpolated to the two stations, and fortunately, at 1-km resolution, stations are located either on model grid points or very close to the grid

points, and therefore, no interpolation from the model grid to the station location was necessary. Monthly averages of the observed maximum, minimum, and average temperatures were calculated over the 11-yr period. Figure 3a shows the monthly average maximum temperature for the Durban and Mount Edgecombe weather stations. The observed lines for Durban and Mount Edgecombe do not converge at any point throughout the year, with maximum temperature in Durban being higher. The CCAM captures the intra-annual temperature cycle, although with some shortcomings. The distinction between the city and rural area is not as clear as in the observations. The Mount Edgecombe maximum temperature is simulated to be higher than in Durban in January, February, and June.

The monthly time series indicates that February is on average the hottest month, with temperatures ranging from 27° to 29°C for both the CCAM and observations at the two stations. The higher temperature during late summer is related to the proximity of the two stations to the Indian Ocean, due to the higher heat capacity of water. July is shown to be the coldest month linked to the Southern Hemisphere winter, but with a temperature range from 22° to 23°C for both the CCAM and observations. There is an increase in temperature from July to December, but with highest temperature range from 25° to 27°C.

The observed maximum temperature is highest at the urban station (Durban) and is higher than the model throughout all 12 months. The CCAM temperature at the urban station is also at least 1°C higher than the observed and CCAM temperature at a nonurban station (Mount Edgecombe). This analysis shows that the CCAM has underpredicted maximum temperature at the urban station and overpredicted maximum temperature at the nonurban station, but only during summer (DJF) and autumn (MAM).

The analysis of minimum temperature is shown in Fig. 3b. As with maximum temperature, minimum temperature is highest during February at both stations, and the model captures this. During summer, the lowest minimum temperature is simulated by the CCAM at a nonurban station, during all months. This modeled temperature is at least 2°C lower than the observed minimum temperature at this station. At the urban station, the CCAM and observed minimum temperatures show a mixed pattern, and the model temperature is higher than observed from March to April, whereas after July, the observed is higher than the model-simulated temperature. At the nonurban station, the CCAM simulation is lower than observed and is also lower than at the urban station. The observed temperature at the nonurban station is also higher than observed at the urban station. The minimum temperature time series shows that the observed temperature is higher than the modeled temperature; this is an indication that the model has underpredicted the minimum temperature and the magnitude of the UHI.

The difference in model simulations and observations between the urban and nonurban stations is shown in Fig. 3c. For maximum temperature, the model produces higher values over the urban station than nonurban station throughout all months, with values between −0.5° and 0.5°C and with negative values during January, February, and June. However, the

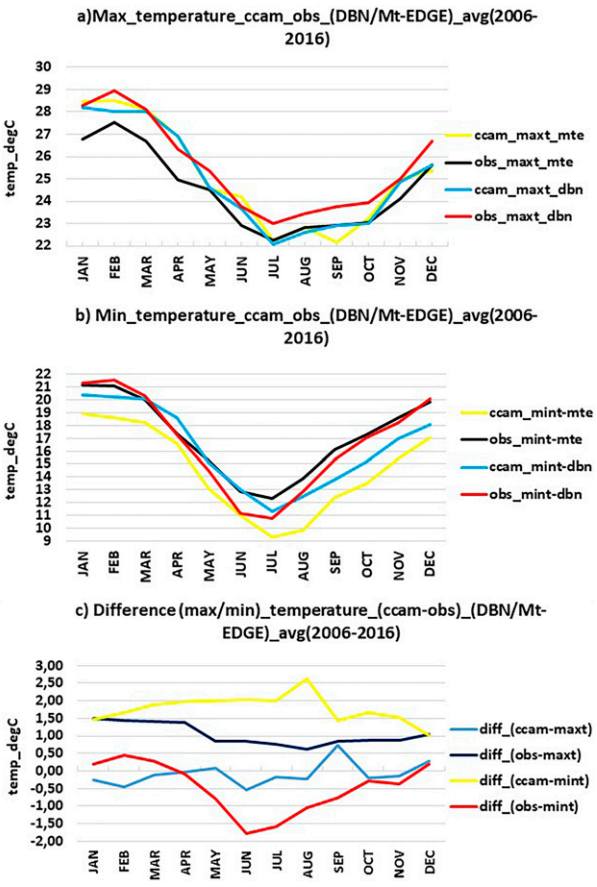

FIG. 3. Comparison between the monthly observed and the CCAM 1-km simulated screen temperatures [(a) maximum, (b) minimum, and (c) average] over the Durban and Mount Edgecombe weather stations for the period 2006–16.

observed maximum temperature is higher at the urban station, with values ranging from 0.5° to 1.5°C and lower values shown during May to August. For minimum temperature, the model produces higher temperature at an urban station, with values ranging from 1.0° to 2.5°C, as compared with a nonurban station; higher temperature values are recorded from January to August. The minimum observed temperature varies between the two stations, with positive difference in the range of 0°–0.5°C between January and April and December. However, the difference is negative from April to October. These values still show that an urban station is warmer than a nonurban station, which could have enhanced the UHI.

The diurnal cycle was also assessed to determine the behavior of temperature between the model and observations during all seasons at the two stations. All of the model output and observations were written out at UTC time before plotting the results (Fig. 4). Figure 4 shows a stronger diurnal variation during summer (DJF) and spring (SON) at the two stations than during autumn (MAM) and winter (JJA), with an average range of approximately 6°C. The model temperature is lower at a nonurban station than at an urban station. Results also show a stronger diurnal variation at a nonurban station than at the urban

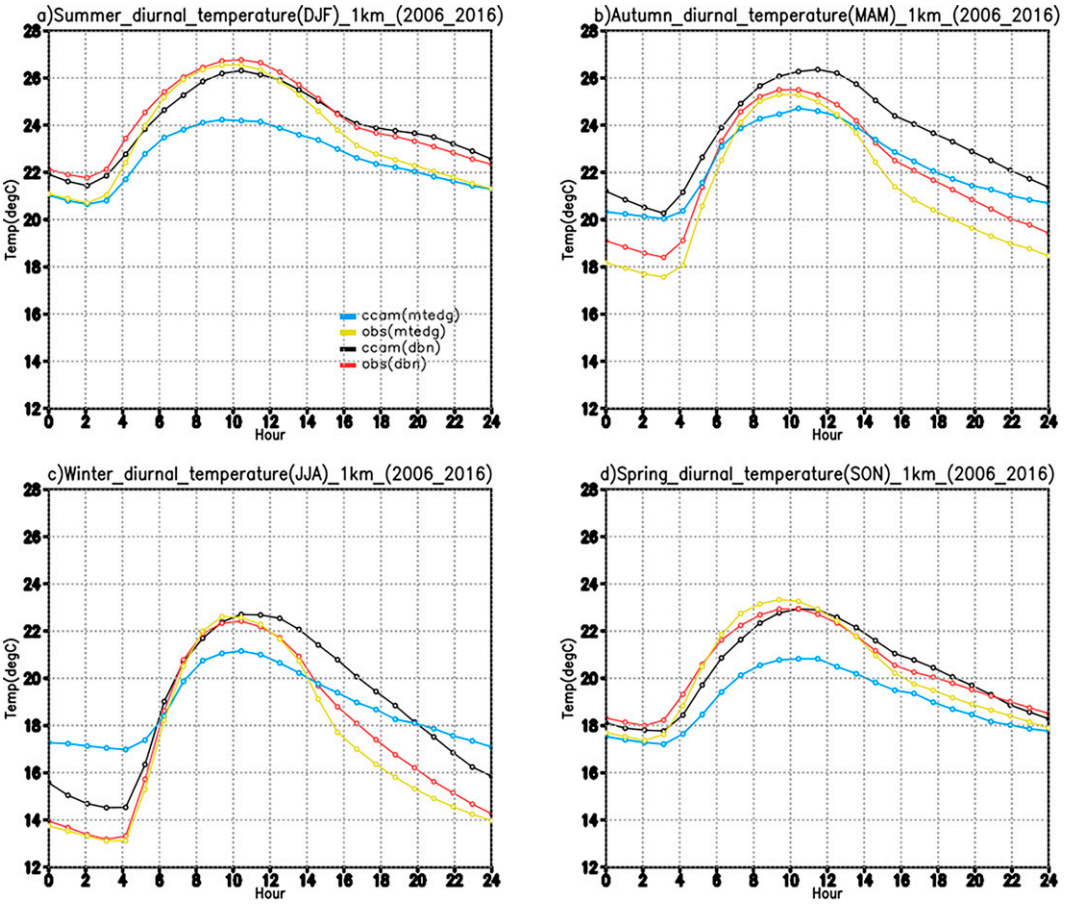

FIG. 4. Seasonal [(a) DJF, (b) MAM, (c) JJA, and (d) SON] diurnal variation in air temperature between the observed and the CCAM at 1-km simulation over Durban and Mount Edgecombe weather stations for the period 2006–16.

station. The autumn diurnal variation is also similar to the summer diurnal range, but with diurnal variation higher than 6°C. Last, winter diurnal variation is weaker, with an average range higher than 8°C. Results show that during DJF (Fig. 4a), the observed temperature starts increasing from around 0200 UTC and reaches the maximum temperature at around 1000 UTC. This tendency coincides with maximum mixing in a convective boundary layer (Efstathiou et al. 2018). The simulated maximum temperature agrees with observation; this also applies to the spring season (Fig. 4d). The diurnal variation at the two stations shows some similarities between the two stations; they are comparable during all seasons.

The stronger summer (DJF) diurnal range provides evidence of the presence of a UHI over the city of eThekwini. The winter (JJA) profile (Fig. 4c) shows a higher diurnal range, with a range higher than 8°C, which is twice that of the summer profile. In the early hours (0000–0400 UTC), the model temperature is higher than observed. From 0400 to 1000 UTC, both the model and observation increase and are similar. After 1000 UTC, the observed temperature decreases faster than the model temperature. The reason could be attributed to the radiation scheme's ability to capture the seasonal variation of the UHI.

During the transition season autumn (Fig. 4b), the diurnal range for the CCAM is at least 6°C, and the observed profile is at least 8°C. The simulated minimum and maximum temperatures are also higher than the observed temperatures throughout the day. This profile is almost similar to the winter (JJA) profile (Fig. 4c).

During the transition season spring, the diurnal range is on average 5°C (Fig. 4d). The spring profile is almost similar to the summer profile (Fig. 4a). This is the season when the UHI starts developing just before it intensifies in summer. When comparing summer and spring, the behavior of the diurnal variation shows similar attributes as in studies by Karl et al. (1993).

The aforementioned study has revealed that within the city, nighttime temperatures are higher due to the presence of the UHI, as a result of surface modifications. This result shows strong correlation between the model and observed, especially during summer and spring. The autumn and winter profiles are also in strong agreement. The higher heat storage capacity (Bohnenstengel et al. 2011) of buildings, surface materials, and pavements leads to an increased storage heat flux during the day (Ramamurthy et al. 2014). At night, the stored heat is released into the atmosphere as sensible heat, which primarily drives higher nighttime temperatures. The decrease

in diurnal variation is attributed to an increase in cloud cover and atmospheric and surface boundary conditions and is a result of global warming and an increase in greenhouse gases (Karl et al. 1993).

The summary of the validation statistics for Durban and Mount Edgecombe stations is shown in Table 2. For minimum temperature, bias is mostly negative and low over Durban and negative but high over Mount Edgecombe. This corresponds to lower RMSE over Durban and higher RMSE over Mount Edgecombe. This applies to the two stations respectively, except during MAM, where bias was positive over Durban and negative over Mount Edgecombe. This result shows that the CCAM underestimates daytime heat storage and its nighttime release, which result in more nighttime cooling, as in the Lemonsu et al. (2023) study.

In maximum temperature, bias is negative and low over Durban, but positive and higher over Mount Edgecombe. However, bias is also on average lower over Durban than over Mount Edgecombe. This result shows that the model underpredicts minimum temperature at both Durban and Mount Edgecombe. The model has also underpredicted maximum temperature over Durban but overpredicted maximum temperature over Mount Edgecombe. These results show that as in Lemonsu et al. (2023), the model performs better in an urban than nonurban station. A bias value less than 1°C indicates very good model performance, and bias is lower in urban than nonurban due to the possibility of the evapotranspiration response of natural areas being enhanced by rainfall (Lemonsu et al. 2023).

2) Comparison of CCAM with MODIS satellite data for 2012/13

This section investigates whether the modeled nighttime UHI phenomenon is also observed by the MODIS satellite and, if so, its spatial and temporal distributions (Fig. 5). The CCAM output was first interpolated to the MODIS grid, and then the spatial correlations between observed and simulated temperatures were calculated. During summer (DJF) months, the CCAM and MODIS nighttime temperatures show almost similar spatial distribution of temperatures, with values higher than 20°C along the east coast over the city of eThekwini. Lower values ranging between 16° and 20°C are simulated away from the city of eThekwini toward the inland. However, the MODIS temperatures are at least 2°C higher than the CCAM temperatures (Figs. 5a,b). Both the CCAM and MODIS correctly reproduce the magnitude and intensity of the UHI, which covers approximately 20 km × 20 km spatial distribution, with an intensity of approximately 4°C temperature difference between rural and urban areas. This agrees with previous studies (i.e., Heaviside et al. 2017; Bohnenstengel et al. 2011). These results agree with those already disclosed or presented based on the Durban (eThekwini) station, which reveals that the simulated minimum temperatures are higher than observed and further indicates that this is a general pattern across the whole high-resolution domain. The temperature distribution resembles the spatial distribution of the urban area observed in the land-cover distribution (Fig. 1), whereby higher temperatures are simulated in highly urbanized areas and lower temperatures are simulated away from urbanized areas.

Table 2. The validation statistics for the Durban and Mount Edgecombe weather station observations against CCAM simulations with ERA-Interim for the period 2006–16.

	Durban		Mount Edgecombe	
	Bias	RMSE	Bias	RMSE
Min temperature				
DJF	−0.83	0.93	−2.51	2.53
MAM	1.29	1.39	−1.58	1.70
JJA	−0.44	0.96	−2.99	3.11
SON	−1.69	1.73	−3.55	3.56
All seasons	−0.42	1.25	−2.66	2.81
Max temperature				
DJF	−0.68	0.81	0.80	1.29
MAM	−0.10	0.53	1.13	1.39
JJA	−0.61	0.72	0.43	0.75
SON	−0.64	0.73	0.10	0.67
All seasons	−0.51	0.62	0.70	1.03

During the autumn (MAM) season, the pattern remains similar to summer, but temperatures are reduced by at least 2° to 4°C (Figs. 5c,d). The UHI intensity is weakened, in the range of 2°C, but with higher temperatures along the coastlines, and it gets reduced farther inland away from highly urbanized areas. The winter (JJA) temperature distribution shows a weakening of the UHI, but it is not completely destroyed. This could be due to anthropogenic heating, which is higher in winter due to increased usage of natural gas and electricity for heating (Coutts et al. 2007). Higher temperatures with values that range between 14° and 18°C are evenly distributed over most parts of eThekwini (Figs. 5e,f). Lower values are depicted over the western half of the domain and away from the city of eThekwini.

During spring (SON), the UHI starts to build up and strengthens; for MODIS, the UHI is almost similar to the one seen in autumn; this observation is in agreement with the Wilby (2008) study, which shows that during spring and summer, the UHI becomes more intense. However, for the CCAM, the UHI intensity is at least 2°C weaker than during autumn, with less magnitude than in MODIS (Figs. 5g,h). In general, the CCAM UHI intensity is at least 2° lower than those of MODIS, this could be due to CCAM underestimating the minimum temperature.

The spatial correlations between MODIS and CCAM were also calculated; summer has the highest correlation (0.90), followed by autumn (0.88), whereas both winter's and spring's spatial correlations are 0.62, respectively. This satellite-derived land surface temperature provides evidence of the spatial and temporal distributions of the UHI simulated by the CCAM.

c. *CCAM simulation of the UHI over the city of eThekwini*

1) UHI seasonal variation from 2005–06 to 2015–16

Improvements in land cover and measured urban settings provide an opportunity to study the temporal and spatial attributes of the UHI. Therefore, in this section, an analysis of

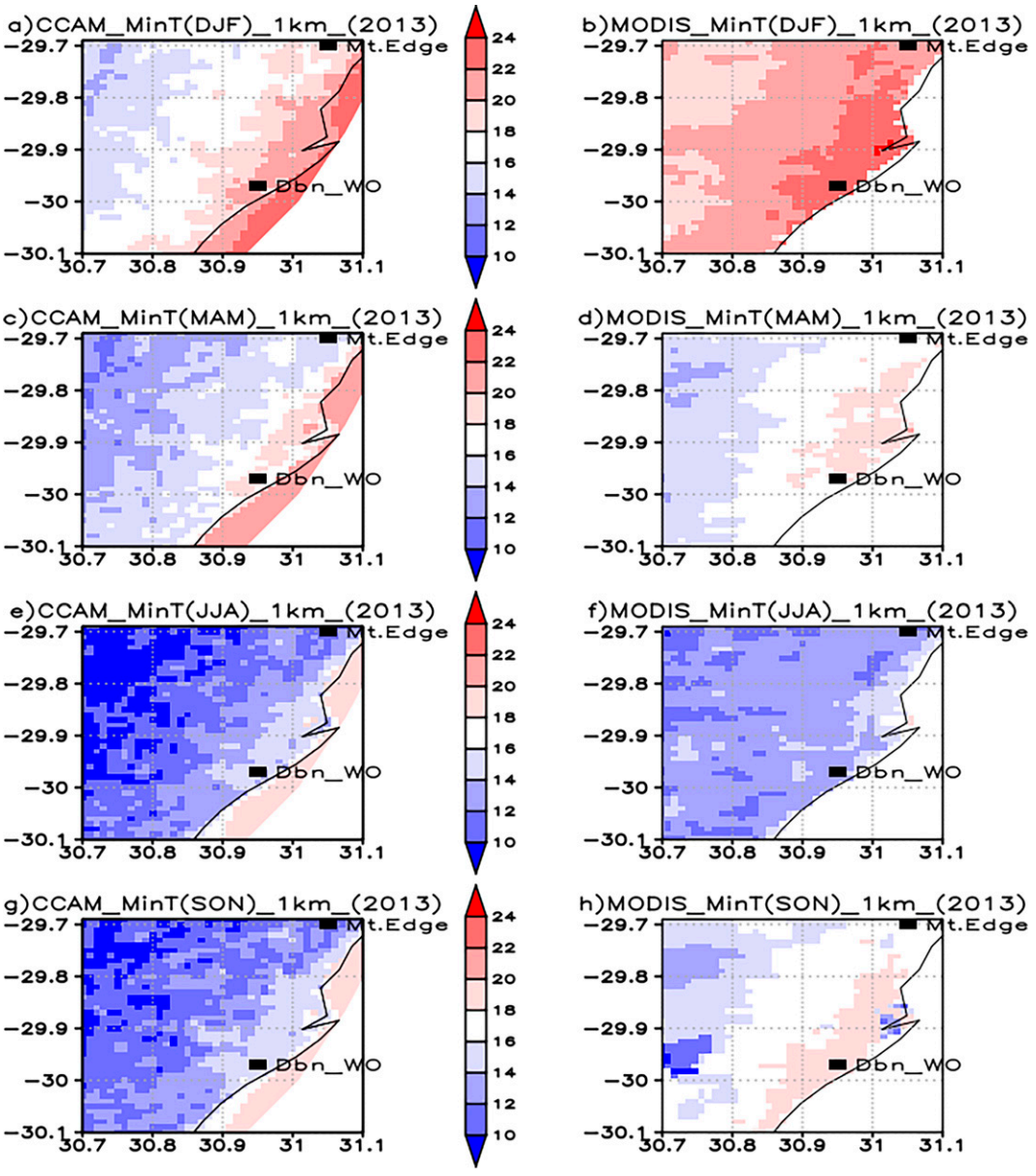

FIG. 5. The (left) CCAM screen and (right) MODIS representation of nighttime temperatures over the city of eThekwini for the periods (a),(b) DJF 2012/13, (c),(d) MAM 2013, (e),(f) JJA 2013, and (g),(h) SON 2013. The validation period concurs with the land-cover data period.

seasonal averages of meteorological variables is performed. The screen maximum temperature simulation is displayed in Fig. 6 and does not reproduce the spatial distribution of the UHI seen in the land-cover (Fig. 1) and urban-fraction graphs (Fig. 2).

During summer, the distribution of screen maximum temperatures shows isolated areas with high values ranging between 28° and 30°C in both urban and rural areas. This also applies to values ranging between 30° and 32°C in both urban and rural areas. There is a decline in maximum temperatures to values lower than 28°C during all other three seasons (autumn, winter, and spring), respectively (Fig. 6). The nonexistence of the UHI in screen maximum temperature confirms that the UHI is a nighttime phenomenon (Chen et al. 2014).

The CCAM-simulated screen minimum temperature is presented in Fig. 7 and surface temperature in Fig. 8. There is a clear difference between the maximum and minimum surface temperatures. The CCAM-simulated screen minimum and surface temperature show the presence of the UHI with spatial distributions similar to those of land cover (Fig. 1) and an urban fraction (Fig. 2). The existence of a UHI intensity is indicated by the clear difference in screen minimum and surface temperature within the city and away from the city.

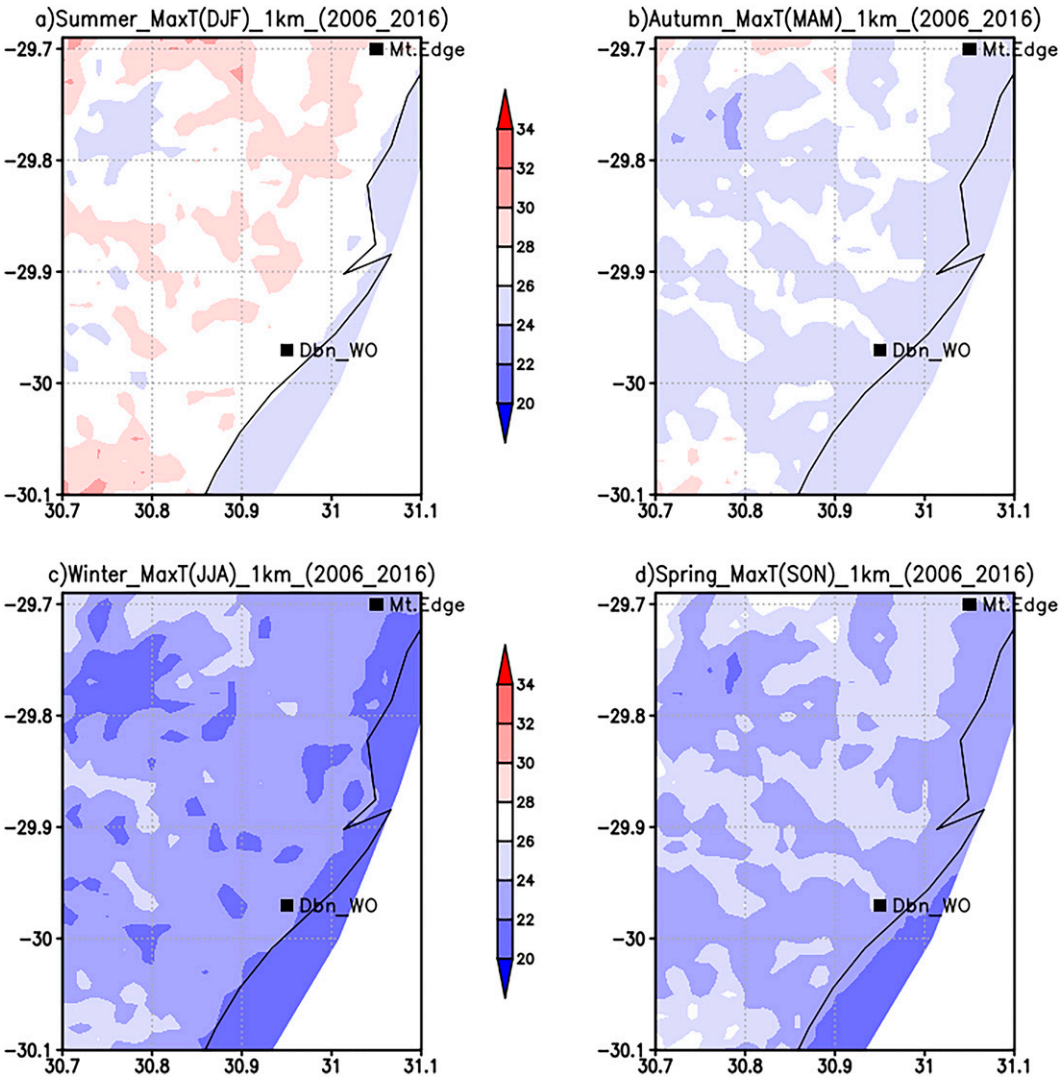

FIG. 6. The updated CCAM 1-km simulated average maximum screen temperature over the city of eThekwini for the periods (a) DJF, (b) MAM, (c) JJA, and (d) SON, from 2005–06 to 2015–16.

The UHI is more clearly simulated during summer, with higher average screen minimum temperatures ranging between 18° and 24°C (Fig. 7a). During the summer season, the UHI intensity has a range of at least 4°C. During autumn and spring, the screen minimum temperatures decrease (Figs. 7b,c), but the UHI remains visible, although weakened; however, its intensity is slightly reduced. The strength of the UHI increases again during spring (Fig. 7d), which is a transition season, to reach a maximum during the summer months.

Observing surface temperatures (Fig. 8), the UHI is stronger during summer, less strong during the transition seasons (i.e., autumn and spring), and weakened during winter because of its seasonal variation (Sannigrahi et al. 2018).

During summer months (DJF), the highest temperature values range from 30° to 32°C along the coast and in some other areas with simulated UHIs. During this season, the UHI spatial coverage is similar to the distribution of land cover (Fig. 1) and urban fraction (Fig. 2), with an intensity at least 4°C, and similar to minimum temperature. As in minimum temperature, the UHI intensity is reduced during autumn and spring. The urban areas are characterized by artificial surfaces with high heat capacity (Akbari et al. 2001; Nuruzzaman 2015), which strengthens the UHI. Note that the surface is cooler away from the UHI as a result of increased vegetation, with higher latent heat fluxes (Garuma 2018) and less sensible heat fluxes in highly vegetated areas (Taha 1997).

The UHI is also evident in net longwave radiation at the surface, where a positive value points upward (Fig. 9), with enhanced values in the urban areas during summer, autumn, and spring seasons. During summer and spring, net longwave radiation ranges from 70 to 80 W m^{-2} within the UHI and is less than 70 W m^{-2} away from the UHI. During autumn, these values are more enhanced to values higher than 80–90 W m^{-2} within the UHI and values less than 80 W m^{-2} away from the UHI.

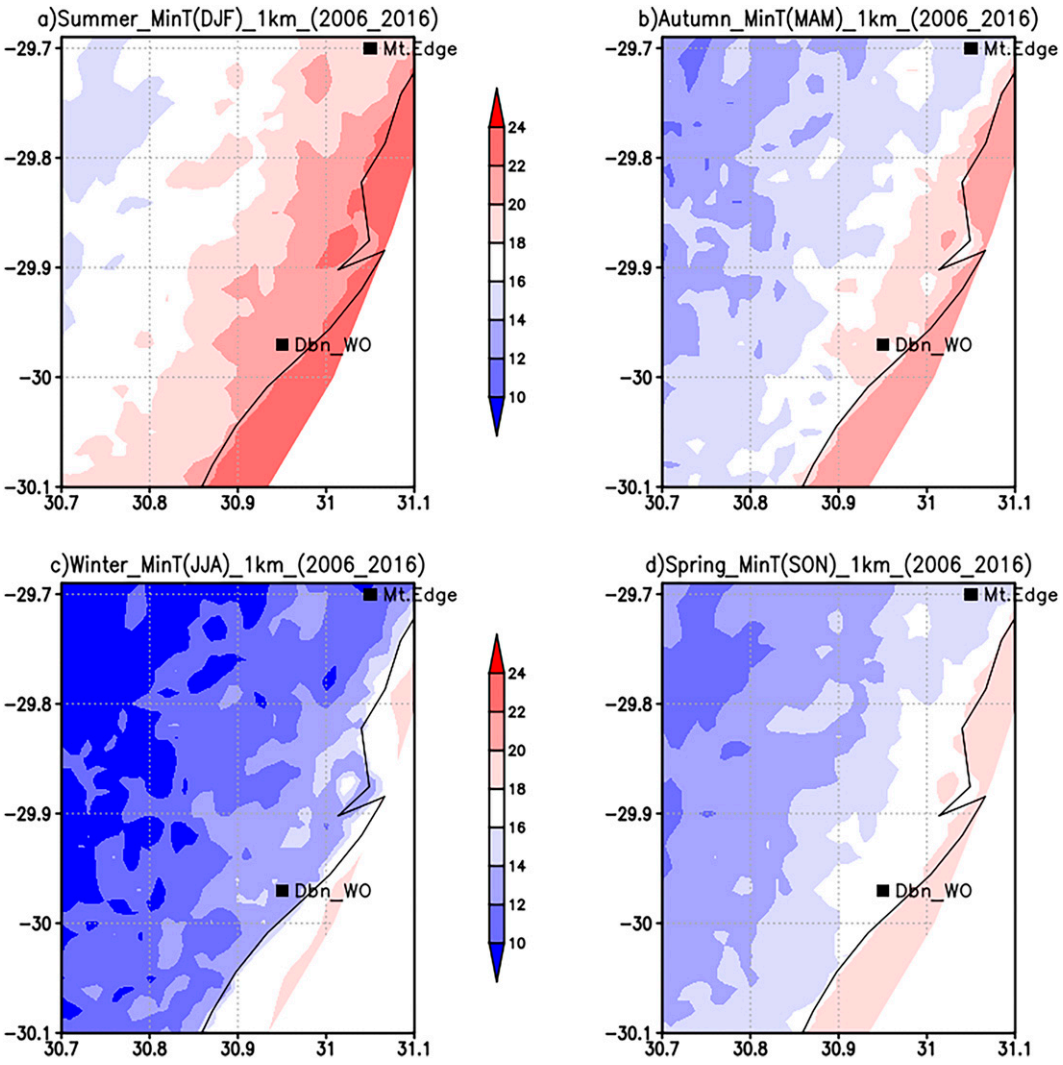

FIG. 7. As in Fig. 6, but for minimum screen temperature.

However, during winter, there is no indication of a UHI, but net longwave radiation values remain high, with a range of 80–100 W m^{-2}. Garuma (2018) attributed higher values of net longwave radiation in cities to both an increased UHI and amplification by pollutants. From this simulation, it is obvious that factors such as high urbanization, low vegetation, anthropogenic heating, and resultant net longwave radiation (Fig. 9) contribute to high minimum and surface temperatures, resulting in the development of a UHI during the summer season.

The distribution of shortwave radiation (not shown) indicates that it is higher in summer over the city, with values higher than 229 W m^{-2}. In autumn, the sun starts migrating northward, leading to shortwave values averaging 160–180 W m^{-2} over the city. In winter, the sun moves to the Northern Hemisphere, leading to values of less than 160 W m^{-2} over the city. The amount of shortwave radiation starts to increase again during autumn as the sun migrates south of the equator again, leading to radiation in the range of 180–200 W m^{-2}, and is slightly higher than in autumn. However, this distribution does not show the presence of the UHI.

Net radiation (not shown), which is the difference between shortwave and longwave, shows an agreement with longwave radiation (Fig. 9). In summer, a UHI is depicted, with net radiation averaging 140–160 W m^{-2} over the city, showing that net radiation is trapped within the city. During autumn, winter, and spring, there is no sign of the UHI. However, net radiation gets reduced in autumn, with lowest values in winter, with averages less than 60 W m^{-2} over the city. However, it strengthens again in spring, with values averaging 120–160 W m^{-2} over the city. The distribution of longwave, shortwave, and net radiation shows proof that the UHI is caused by natural factors such as the distribution of radiation within urban areas.

The distribution of sensible heat flux (not shown) shows the distribution of the UHI during all four seasons. In summer, sensible heat flux averages 100–140 W m^{-2} over the city. This is opposed to latent heat flux, with values less than 60 W m^{-2}.

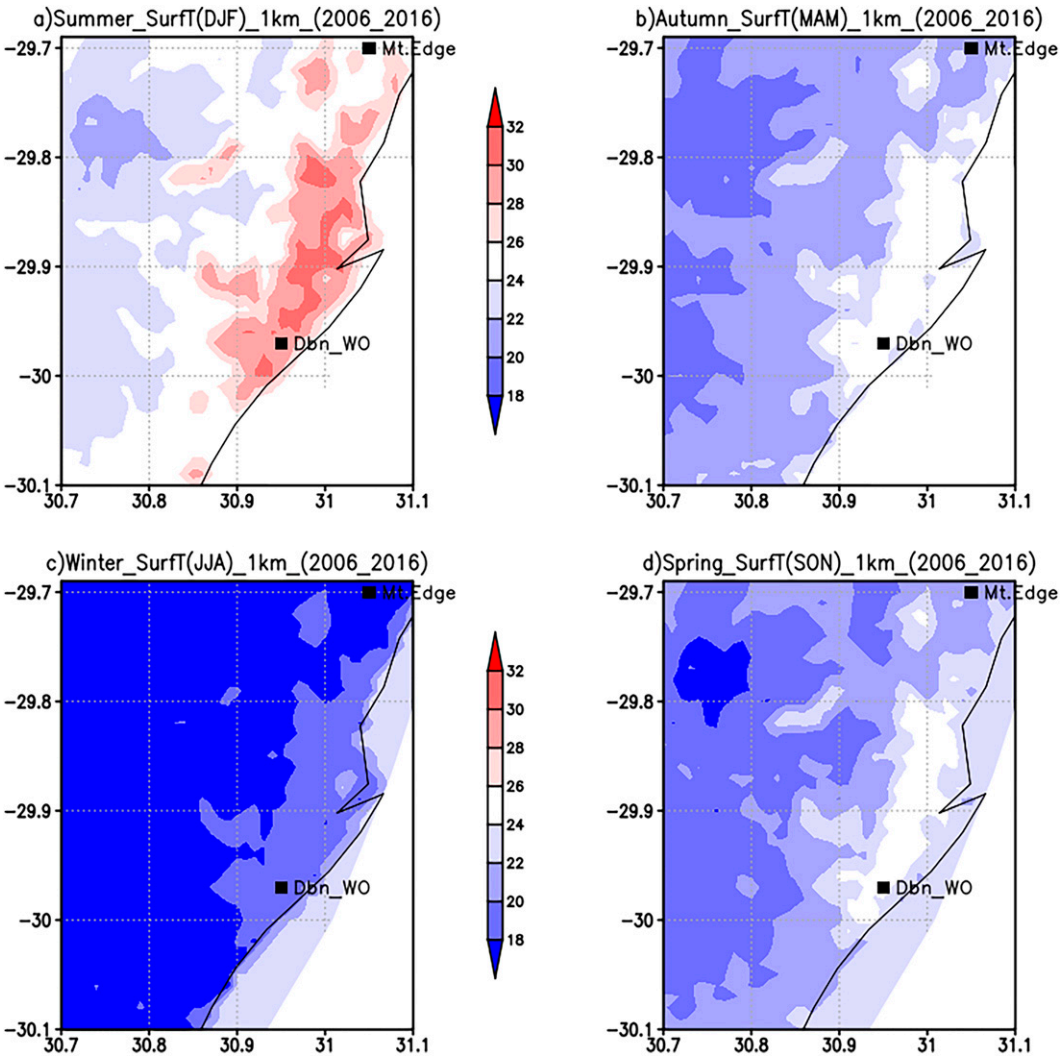

FIG. 8. As in Fig. 6, but for surface temperature.

Sensible heat is reduced to values of 60–80 W m^{-2} during autumn. During this season, latent heat flux remains similar to summer values. Sensible heat flux is reduced to its lowest values, less than 40 W m^{-2}, during winter. This is accompanied by the lowest values of latent heat flux, which averages 40–60 W m^{-2}. During spring, sensible heat increases again to average values of 60–100 W m^{-2}, but latent heat fluxes remain low, with values similar to the summer profile.

The distribution of sensible heat shows that it is enhanced by anthropogenic heating as it opposes the distribution of latent heat flux. There is not much increase in latent heat during all seasons, meaning less evaporation, an indication that there is less water available for evaporation, thus enhancing sensible heat flux. Therefore, this result presents evidence that the UHI is also caused by anthropogenic heating.

Vegetation fraction (not shown) was also analyzed for the four seasons and compared with urban fraction. In summer, it shows that areas located over the city have vegetation fraction less than 50%. This area is dominated by urban fraction higher than 90%. As one moves away from the city, urban fraction is reduced to less than 10%, and vegetation fraction increases to more than 60%. The distribution of vegetation fraction in summer and autumn seasons remains similar. During winter, most parts of the domain have vegetation fraction less than 50%, with very small areas away from the city with vegetation fractions in the range of 60%–70%. This is almost similar to vegetation distribution during spring, but there is a slight increase in vegetation fraction of 50%–60% in some areas away from the city.

2) UHI SEASONAL DIURNAL VARIATION FOR 2005–06 TO 2015–16

In this section, the seasonal diurnal variation of surface variables is analyzed. This examination indicates a 24-h variation of the meteorological variables over the city. Figure 10 shows the diurnal variation of surface temperatures, boundary layers, net longwave and net shortwave radiation, and latent

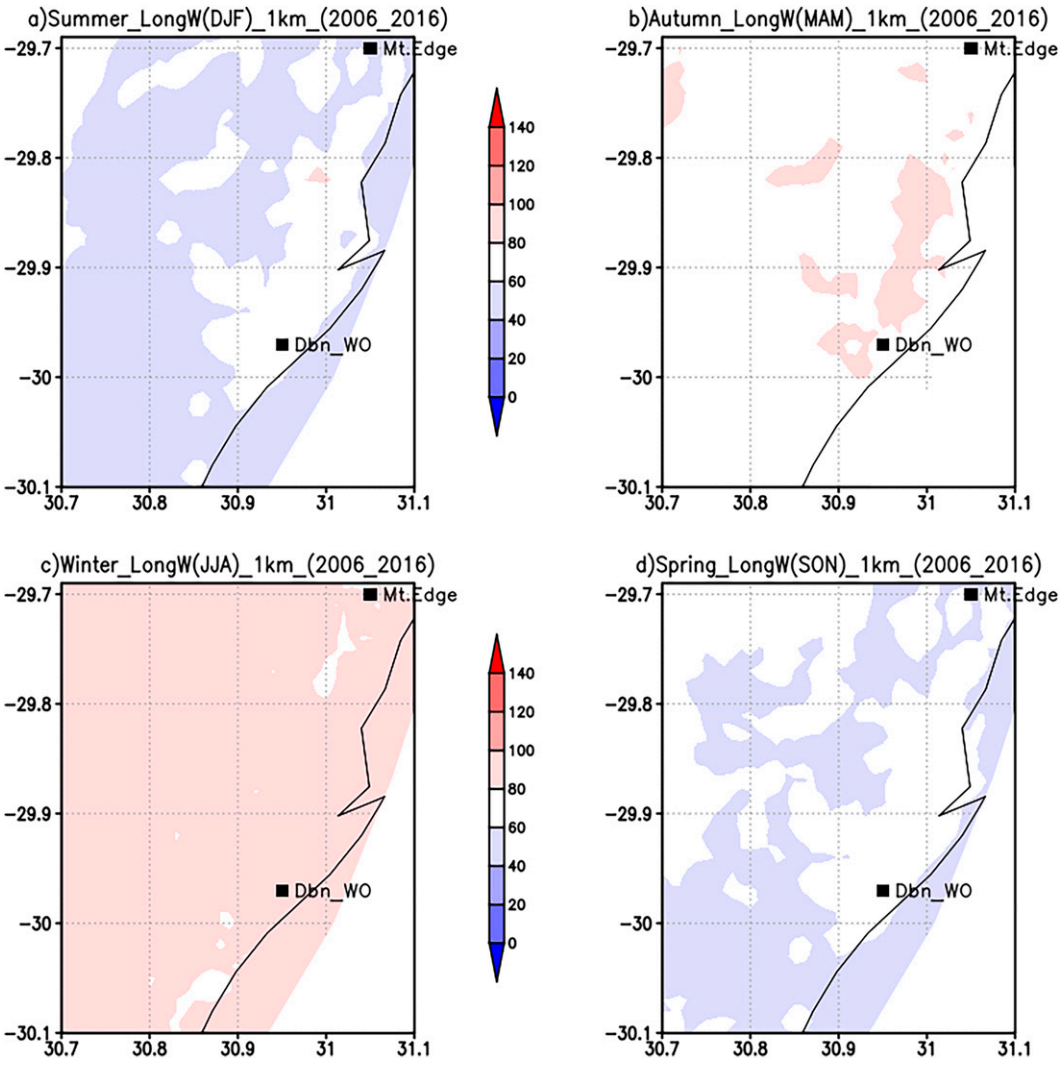

FIG. 9. As in Fig. 6, but for net longwave radiation at the ground (positive is up).

and sensible heat fluxes, respectively. The surface temperature profile shows a similar diurnal variation pattern during all seasons (Fig. 10a), but with various strengths. The summer and autumn profiles are almost similar and are stronger (less variation) than the winter and spring profiles, respectively. The summer and autumn profiles have a range of at least 8°C, whereas the winter and spring profiles have a range of at least 10°C, respectively. The summer and autumn profiles are at least 3°C higher than the spring profile and at least 5°C higher than the winter profile. All these profiles show that during late hours (after 1600 UTC), excess heat is not released by the surface, which contributes to the UHI. Kruger and Shongwe (2004) attributed negative diurnal variation of temperature in stations over South Africa to increasing minimum temperature (hot/warm nights) because of urbanization. Also, Karl et al. (1993) and Hughes and Balling (1996) mentioned that over South Africa, diurnal variation of temperature strongly decreases in spring and strongly increases in autumn as a result of an increase in nighttime temperature. An increase in gases such as CO_2, sensible heat fluxes, and evaporation reduce the diurnal range of temperature (Karl et al. 1993). The current CCAM results agree with previous findings (e.g., Hughes and Balling 1996) that increased urbanization is responsible for the reduction in diurnal variation of temperature.

The daytime variation of the planetary boundary layer is depicted in Fig. 10b, whereby profiles are similar during all seasons. However, the DJF profile is at least 100 m less than other profiles. The diurnal variation ranges from 350 to 400 m in the morning and between 850 and 1000 m in the afternoon, leading to a range of approximately 600–650 m. The diurnal variation of net longwave radiation at the ground (positive, up) is shown in Fig. 10c. Its diurnal range is strongest in summer, with the lowest range of 35 W m^{-2}. This is followed by the transition seasons autumn and spring, with a range of 40 W m^{-2}. Winter has the highest diurnal variation, with a range of 40 W m^{-2}. The diurnal variation of sensible and latent heat fluxes is, however, not shown. For sensible heat fluxes, a strong variation exists during spring, with a range of ±170 W m^{-2},

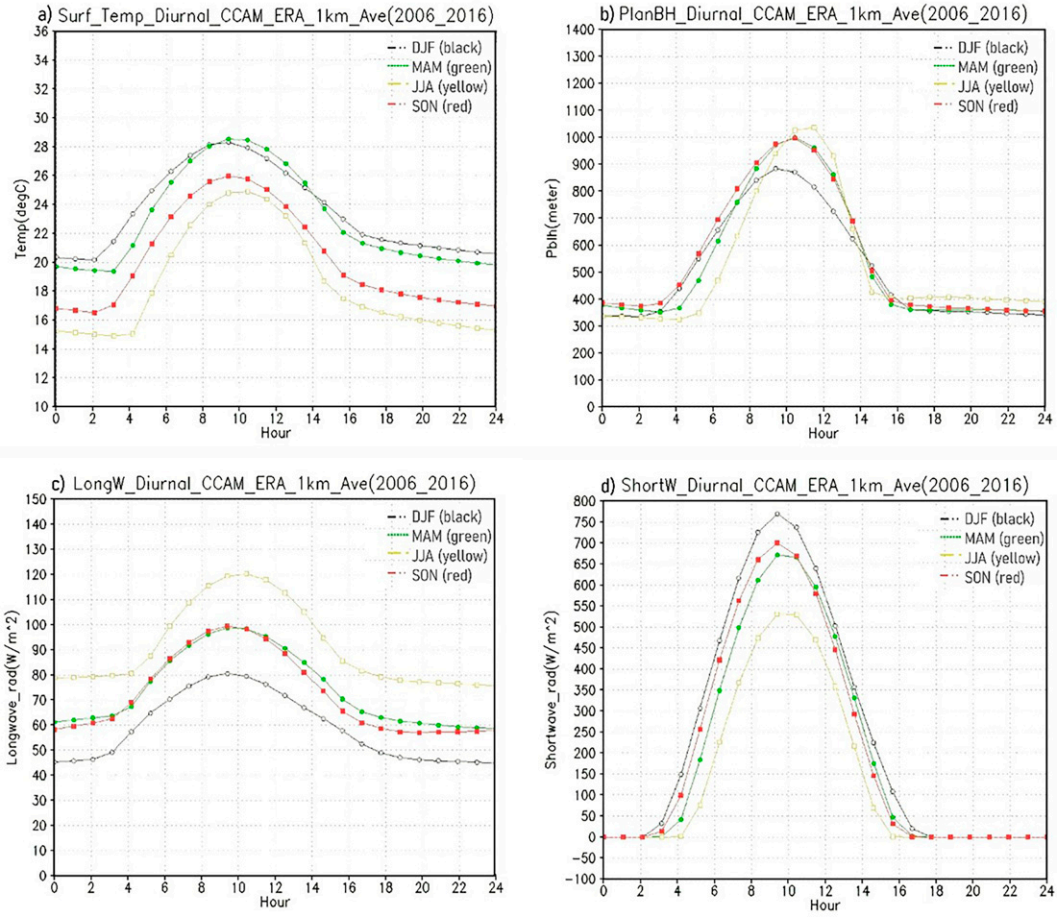

FIG. 10. The updated CCAM 1-km simulated diurnal variation of (a) surface temperature, (b) boundary layer profile, (c) net longwave at the ground (positive is up), and (d) net shortwave radiation at the ground (positive is down) over the city of eThekwini for the periods DJF, MAM, JJA, and SON, from 2005–06 to 2015–16.

followed by summer (±40 W m^{-2}), autumn, and lastly winter (<130 W m^{-2}).

For latent heat, the diurnal cycle varies with seasons, with a strong variation during summer (75–210 W m^{-2}; range is ±135 W m^{-2}), followed by a less significant variation in autumn (100–200 W m^{-2}; range is 100 W m^{-2}) and spring (85–170 W m^{-2}; range is 85 W m^{-2}), and last a minor variation in winter (100–150 W m^{-2}; range is 50 W m^{-2}). For both the sensible and latent heat fluxes, all the values are lower than values found in Luhar et al. (2014). Changes in diurnal variation have been attributed to increased cloud cover and its changes since it reduces incoming solar radiation during the day, which reduces maximum temperature and increases net longwave radiation at night, increasing nighttime temperature and reducing its diurnal variation (Easterling et al. 2000). Kruger et al. (2019) found that changes in minimum and maximum temperatures affect diurnal variations as a result of the influence of either local or microscale climate.

All of these simulation results confirm the presence of a nighttime UHI over the city of eThekwini during summer, whereby the ground and building materials hold onto more solar energy during the day (Lipson et al. 2017), instead of releasing it, with a lower rate of radiant cooling at night (Wilby 2008). Equally, the availability of anthropogenic heating from air conditioners increases heat in the cities. However, the existence of atmospheric circulations such as sea breezes could have reduced the strength of the UHI. Of interest was that the 2015–16 seasons experienced the strongest El Ñino over the 11-yr period (Blamey et al. 2018). Therefore, there might be a relationship between the UHI and El Ñino, as El Ñino is known to lead to reduced rainfall and almost certainly higher surface temperatures. From this comparison, it is shown that the current CCAM setup is capable of simulating the urban climate of eThekwini and could be applied in future simulations.

4. Discussion

In this study, the climate of the UHI during the period 2005–16 is discussed. The UHI was simulated by the CCAM, coupled to the land surface model, called CABLE. The CCAM-CABLE allows for the user to change land cover; the system has an option of 17 IGBP vegetation classes ranging from water bodies to various land-cover types. CABLE includes

an option to apply measured urban parameters, such as building characteristics, emission sources, and reflectivity.

The land cover was updated to reflect land use on the ground. The updated land-cover and urban parameters were found to have an influence on UHI intensity. First, when the model was run with the default land cover and urban setting switched on, there were no dynamical changes in vegetation throughout the season and no dynamical changes in the simulated UHI. Second, when the land cover was updated and urban setting switched off, the UHI was not reproduced; there were no dynamical changes in vegetation throughout the season, and no distinguished UHI was simulated. In this study, it is shown that the city is 90% urban and is considered dense urban (Lemonsu et al. 2023); vegetation cover is lower, and there are more impervious materials, which increases the UHI and its intensity, which agrees with previous findings (e.g., Sannigrahi et al. 2018). Therefore, increasing vegetation, ventilation, and greening of urban spaces (Heaviside et al. 2017; Zhang et al. 2022) improve the development of daytime boundary layers since they alter the surface energy balance (Sharma et al. 2016), cool the urban space, and increase evapotranspiration. In cities, sensible heat and heat storage dominate in summer, and latent heat is small, which influences the UHI (Coutts et al. 2007). More vegetation within the canyon (in-canyon vegetation) helps with reducing urban temperatures, as vegetation absorbs both longwave radiation and sensible heat fluxes from roads and walls, thereby increasing latent heat (Thatcher and Hurley 2012).

In this study, albedo from roofs, walls, and roads is similar to the default albedo (0.2); an increase in albedo should decrease the intensity of the UHI. Previous studies have shown that darker materials cause an increase in surface temperatures in cities (Nuruzzaman 2015), with temperatures at least 2°C higher than in rural areas (Taha 1997; Garuma 2018; Chapman et al. 2019). The application of lighter and brighter colors increases the albedo to values higher than 0.25, which could, therefore, reduce temperatures by at least 4°C in cities (Garuma 2018; Taha 1997), thereby eliminating the UHI and reducing energy demand for both heating and cooling. Colors that are heat resistant could be applied to roofs to provide the necessary cooling. Alternatively, rubber materials could be used at no extra cost instead of changing colors. For this study, albedo was lower than 0.25, which could have helped in reducing the UHI intensity. Previous studies have shown that the impact of emissivity on the thermal behavior of urban materials is greatest at night, and reflectivity is more relevant during the day (Synnefa et al. 2006). For this study, both emissions from industries and traffic were higher than in the default model setup; such an increase in anthropogenic emission results in higher temperatures in urban areas, strengthening the UHI intensity.

The city is located over the east coast of South Africa and is bounded by the warm Indian Ocean. Previous studies have shown that the proximity of cities to water bodies such as lakes and the ocean results in the development of sea or lake breezes, which act as UHI-mitigating factors (Sharma et al. 2016). In this study, we found the UHI has an intensity in the range of 2°–4°C, and in large cities, the UHI intensity could range from 5° to 10°C (Heaviside et al. 2017; Grimmond et al. 2011); therefore, the ocean could have played a role in reducing the UHI intensity.

The study shows that the CCAM is able to capture the spatial and temporal distributions of the UHI by reproducing the times series of seasonal variation of temperatures over both nonurban and urban stations in the eThekwini municipality. The results also indicate that the highest average monthly temperature is observed and simulated in February. February represents the end of summer in the Southern Hemisphere due to the latitudinal variation of the position of the sun. The proximity to the warm Indian Ocean is also thought to have an influence on the temperature in eThekwini in both the urban and rural settings. The observed temperature is higher at the urban station during summer, with a range of 0°–0.5°C for minimum temperature and 0.5°–1.5°C for maximum temperature.

The diurnal variation is strongest during summer, especially at the urban station as compared with the nonurban station, with an average range of 6°C, and is almost similar to the one in spring before the UHI strengthens again. During July, the temperature is the lowest, when the city receives the lowest radiation as the sun moves to the Northern Hemisphere in winter. The diurnal range in winter is weakest, with an average of 8°C or more, and is almost similar to the autumn profile. Still, an urban station shows higher values as compared with a nonurban station.

The comparison between CCAM and MODIS data also shows that during summer the UHI intensity is on average 4°C between urban and rural. The UHI intensity is reduced during all other seasons, although MODIS temperature is warmer than CCAM. Likewise, the highest correlation was found between MODIS and simulated minimum temperatures in summer.

The CCAM simulation of maximum temperatures did not provide any evidence of a UHI. The reason could be that daytime temperatures are dependent on the amount of received shortwave radiation and topography, where higher temperatures develop in low topography and low temperatures in higher topography (Maisha 2014). Also, the convective boundary layer or turbulent exchange in the near-surface layer during the day contributes to the dissipation of the UHI (Zhang et al. 2022).

The current CCAM climate simulations of surface parameters such as temperature (minimum and surface), longwave radiation, and boundary layer profile provide evidence of the existence of the UHI over the city of eThekwini. The magnitude of the area covered by the UHI stretches about 20 km (west to east) and 20 km (south to north) and is similar in distribution to land cover and areas that are more than 80% urbanized.

In minimum temperature simulation, the UHI intensity shows its dominance during summer, where the city temperature is on average 4°C more than in rural areas. This is in agreement with findings by Wilby (2008). This pattern is also shown in surface temperature, but with a slightly different intensity pattern shown in minimum temperature. This is shown by the more intense UHI seen away from the ocean, which could be due to the effects of land and sea breezes, which have diluted the UHI closer to the coastline. The UHI is then weakened during autumn and spring and is almost nonexistent

during the winter season. The UHI is oriented in a southwest-to-northeast orientation, most distinguished along the coastal area, and resembles the distribution of both the land cover and the urban fraction.

The UHI also follows the pattern depicted by the longwave radiation, especially during summer; this is the result of shortwave radiation being trapped by urban structures as longwave radiation and not released at night. The distribution of longwave radiation has led to an increase in both surface and minimum temperatures, with the UHI intensity of urban temperatures at least 4°C higher than in rural areas (Grimmond et al. 2011; Heaviside et al. 2017), also in agreement with studies by, for example, Taha (1997) and Garuma (2018). Away from urban areas, there is an increase in vegetation and a reduction in artificial materials, thereby reducing both the surface and minimum temperatures. There is also increased evapotranspiration, and trees absorb more carbon dioxide. Large tree canopies help in reducing heat as they intercept light (Nuruzzaman 2015), thereby reducing the UHI.

An analysis of diurnal variation of various meteorological variables such as temperature, boundary layer, longwave and shortwave radiation, and sensible and latent heat fluxes confirms the strength of the UHI. In summer, the diurnal variations of temperature, boundary layer, longwave radiation, and sensible heat fluxes are strongest.

From this study, two elements that contributed to the development of the UHI were identified: (i) natural factors and (ii) man-made factors. With natural factors, the distribution of longwave radiation was identified (Coutts et al. 2007), whereby an increase (decrease) in radiation was found to enhance (reduce) the development and the strength of the UHI. Also, regional atmospheric circulations could have played a role in the enhancement of the UHI. Blamey et al. (2018) indicated that the El Niño climate pattern (with unusual warm ocean waters) dominated the South African weather during the year 2015/16. It impacts moisture transport over the region, whereby the weakening of onshore moisture flow over the south Indian Ocean contributes to dry conditions (Blamey et al. 2018). Man-made factors including urban expansion and increased anthropogenic heating within the city influenced the spatial and temporal distributions of the UHI (Wang and Li 2017; Coutts et al. 2007).

These simulations have shown that an increase in both spatial and temporal resolutions improved the spatial distribution of the UHI. On average, the formation of a UHI was not very strong; it has an average of 4°C. Heaviside et al. (2017) and Bohnenstengel et al. (2011) have shown that the UHI intensity is between 5° and 10°C in larger cities, but also in extreme cases. This could be due to the location of the city, which is located along the warm east coast of South Africa, along the warm Indian Ocean. In this case, mesoscale circulations could result in the development of sea breezes. Such circulations are dominant mesoscale systems over coastal areas and are responsible for the dilution of the UHI (Taha 1997; Pokhrel and Lee 2011; Lehoczky et al. 2017; Arrillaga et al. 2018). Also, water bodies provide evaporation and reduce surface temperatures. Taha (1997) indicated that in higher latitudes the UHI reduces energy demand for heating as compared with lower-latitudinal areas since UHI increases lead to higher demand for cooling systems.

The current study has shown that the CCAM is able to reproduce the UHI over eThekwini as it captures the spatial and temporal distributions of the UHI. The UHI was found to be caused by factors such as increased urbanization, increased greenhouse gas emissions, reduced vegetation in cities, and climatic conditions (Nuruzzaman 2015). The current study has also proven that the CCAM system could be used as a tool to model urban climate at any geographical location around the globe and at any time scale. The current model configuration and results, therefore, support earlier findings by Reichler and Kim (2008), who attributed climate model performance to developments such as more realistic model parameterizations and finer resolution.

According to previous studies, as a result of increased urbanization, there is an increase in the Bowen ratio, because sensible heat fluxes increase (because of strong surface heating) as compared with latent heat fluxes, as a result of a reduction in surface moisture (Coutts et al. 2007), as well as the replacement of natural vegetation by artificial surfaces (Ramamurthy et al. 2014). This has also resulted in the enhancement of the UHI.

The current study is essential because the occurrence of UHIs in cities has a catastrophic impact on human lives, and therefore, this kind of study assists city planners when developing modern cities. Therefore, it enables researchers in urban climate studies to understand how atmospheric circulations impact city climates. The UHI is due to both natural factors and anthropogenic emissions; therefore, numerical and climate modelers could use this study to understand that radiation parameters and emissions from cities, along with urban modification, including removal of natural surfaces, are important in physical parameterization.

In this study, there were some limitations, which are listed as follows. The study area has limited observation stations and incomplete data, which limit the study. When the CABLE parameters were changed from default to the updated/measured, the realistic orientation of the city is updated, as well as the dynamic change of vegetation with cites. This was, however, not correctly shown in default land cover. Therefore, for urban modeling, not having the required and latest land-cover data impacts the results of the modeling studies. In Africa, this dataset is, however, not so easy to find, except from large global centers. Therefore, in this study, we made an effort to get these measured data and customize them for the CCAM-CABLE to read before preparing surface parameters. Another limitation to this study is that UCM allows for only one class of urban parameter to represent the entire grid during simulations. Therefore, due to the complexity of urban-scale simulation, large computing resources are required to successfully complete the model runs. The urban model study requires large computing resources, and for countries without such computing resources, this has a detrimental effect on high-resolution modeling studies.

From the current studies, the realistic simulation of the UHI with ERA-Interim provides an opportunity to run the model at high resolution and project the future occurrence of the UHI using CMIP5 and CMIP6. Such future projections will be used to assist disaster management with the dissemination of information

on extreme weather and climate events over the cities. However, it is important for the modelers to update the land-cover and urban parameters to realistically simulate city climate in future.

5. Conclusions

The study was aimed at evaluating the performance of the CCAM 1-km setup in simulating the UHI over the city of eThekwini during the current climate (2006–16). The CCAM setup at 1 km was coupled to a land surface model (CCAM-CABLE), which takes into consideration updated land-cover and measured urban parameters. During the simulations, the urban scheme was turned on. The two changes allowed for a realistic simulation of the UHI: (i) the updated land-cover data, which assist in capturing the true seasonal variability of vegetation as compared with the default setup, which shows no such variability, and (ii) the measured urban parameters, where a generic option was selected. The measured parameters allow for realistic simulation of UHI intensity; an overestimation of these values could have resulted in greater UHI intensity, such as in a medium urban or highly urbanized city. All these parameters show the true spatial distribution of the city, located along the warm east coast of South Africa, as compared with the default setup. The city is located at approximately 29.9°S, which is very close to the subtropical high-pressure belt (30°S). The urban fraction shows that the city is more than 80% urbanized and covers an area of around 20 km × 20 km.

The monthly variation of temperature shows that the CCAM underforecast the average maximum temperature by at least 2°C and overforecast the average minimum temperature by at least 3°C when compared with observation. An analysis of temperature diurnal variation shows that it is strong in summer, with a range between maximum and minimum values of around 6°C due to UHI intensity.

Comparison between CCAM and MODIS temperature values shows the UHI intensity is at least 4°C higher in urban areas than rural areas during summer. This in in agreement with previous studies such as Grimmond et al. (2011) and Heaviside et al. (2017). The UHI intensity is reduced in autumn and winter but starts growing during spring, and this is in agreement with a study by Zhang et al. (2022).

The CCAM climate simulations show no UHI in daytime maximum temperature, as this is a nighttime event. The UHI is shown in minimum and surface temperatures during summer; its intensity is at least 4°C. The UHI intensity is also seen in longwave radiation during summer, with a difference of at least 10 W m^{-2} in urban as compared with rural. The UHI spatial distribution is similar to the urban fraction and land-cover distribution. The UHI also exists during both autumn and spring, but with reduced intensity; however, it gets reduced during the winter season.

This study shows that both shortwave and longwave radiation play a role in the development, spatial distribution, and intensity of the UHI. Since shortwave is received at the surface during the day, it gets absorbed in cities, and during nighttime, longwave radiation is released back into the atmosphere. However, this study shows that longwave radiation is only reduced in rural areas and is retained by urban surfaces, including roads and buildings in cities. The combination of longwave radiation and anthropogenic heating raises the surface temperature and increases the intensity of the UHI. In this study, we can conclude that changes in land cover and urban parameters have assisted in simulating and identifying the UHI over the city of eThekwini.

Results of this study will further assist the municipality in deriving strategies to mitigate the impacts of climate change and also for modern urban design. This includes the use of materials with high reflectivity or emissivity, as they promote cooler surfaces (Taha 1997); green spaces; and water features (Wilby 2008; Heaviside et al. 2017; Zhang et al. 2022).

Future research studies will include simulation of the projected urban climate of eThekwini and the occurrence of the UHI under enhanced anthropogenic emissions using the different emission scenario data from the IPCC report and assessment of the influence of atmospheric flow dynamics such as land and sea breezes in the distribution of a UHI. We also recommend that similar studies be conducted over other South African cities to help the government with its implementation of the District Development Model.

Acknowledgments. The authors thank the Water Research Commission (Project C2020/2021-00596) who funded publication of this research. They also acknowledge the eThekwini municipality for supporting the study and for the urban-parameter data. The authors thank the Council for Scientific and Industrial Research (CSIR) for the usage of the Centre for High Performance Computing (CHPC) for model runs and the CSIR, the University of Pretoria, and the South African Weather Service (SAWS) for the academic support. The authors also thank the South African Weather Service for station data used to validate the model. They acknowledge Ms. Ingrid Booysen for her English editing.

Data availability statement. The ERA-Interim data used for the study are originally saved in a Network Common Data Form (netCDF) and are available on the CSIRO website. MODIS data can easily be ordered by date, time, and location, and the SAWS observations provided for this study can be acquired after signing a disclosure form.

REFERENCES

Akbari, H., M. Pomerantz, and H. Taha, 2001: Cool surfaces and shade trees to reduce energy use and improve air quality in urban areas. *Sol. Energy*, **70**, 295–310, https://doi.org/10.1016/S0038-092X(00)00089-X.

Arakawa, A., 2004: The cumulus parameterization problem: Past, present, and future. *J. Climate*, **17**, 2493–2525, https://doi.org/10.1175/1520-0442(2004)017<2493:RATCPP>2.0.CO;2.

Arrillaga, J. A., J. V. G. de Arellano, F. Bosveld, H. K. Baltink, C. Yagüe, M. Sastre, and C. Román-Cascón, 2018: Impacts of afternoon and evening sea-breeze fronts on local turbulence, and on CO_2 and radon-222 transport. *Quart. J. Roy. Meteor. Soc.*, **144**, 990–1011, https://doi.org/10.1002/qj.3252.

Baklanov, A., and Coauthors, 2018: From urban meteorology, climate and environment research to integrated city services. *Urban Climate*, **23**, 330–341, https://doi.org/10.1016/j.uclim.2017.05.004.

Barrao, S., R. Serrano-Notivoli, J. M. Cuadrat, E. Tejedor, and M. A. Saz Sánchez, 2022: Characterization of the UHI in Zaragoza (Spain) using a quality-controlled hourly sensor-based urban climate network. *Urban Climate*, **44**, 101207, https://doi.org/10.1016/j.uclim.2022.101207.

Blamey, R. C., S. R. Kolusu, P. Mahlalela, M. C. Todd, and C. J. C. Reason, 2018: The role of regional circulation features in regulating El Niño climate impacts over southern Africa: A comparison of the 2015/2016 drought with previous events. *Int. J. Climatol.*, **38**, 4276–4295, https://doi.org/10.1002/joc.5668.

Bohnenstengel, S. I., S. Evans, P. A. Clark, and S. E. Belcher, 2011: Simulations of the London urban heat island. *Quart. J. Roy. Meteor. Soc.*, **137**, 1625–1640, https://doi.org/10.1002/qj.855.

Bozonnet, E., R. Belarbi, and F. Allard, 2007: Thermal behaviour of buildings: Modelling the impact of urban heat island. *J. Harbin Inst. Technol.*, **14**, 19–22.

Chapman, S., M. Thatcher, A. Salazar, J. E. M. Watson, and C. A. Mcalpine, 2019: The impact of climate change and urban growth on urban climate and heat stress in a subtropical city. *Int. J. Climatol.*, **39**, 3013–3030, https://doi.org/10.1002/joc.5998.

Chen, D., M. Thatcher, X. Wang, G. Barnett, A. Kachenko, and R. Prince, 2015: Summer cooling potential of urban vegetation—A modeling study for Melbourne, Australia. *AIMS Environ. Sci.*, **2**, 648–667, https://doi.org/10.3934/environsci.2015.3.648.

Chen, F., and Coauthors, 2011: The integrated WRF/urban modelling system: Development, evaluation, and applications to urban environmental problems. *Int. J. Climatol.*, **31**, 273–288, https://doi.org/10.1002/joc.2158.

——, X. Yang, and W. Zhu, 2014: WRF simulations of urban heat island under hot-weather synoptic conditions: The case study of Hangzhou City, China. *Atmos. Res.*, **138**, 364–377, https://doi.org/10.1016/j.atmosres.2013.12.005.

Cook, C., C. J. C. Reason, and B. C. Hewitson, 2004: Wet and dry spells within particularly wet and dry summers in the South African summer rainfall region. *Climate Res.*, **26**, 17–31, https://doi.org/10.3354/cr026017.

Coutts, A. M., J. Beringer, and N. J. Tapper, 2007: Impact of increasing urban density on local climate: Spatial and temporal variations in the surface energy balance in Melbourne, Australia. *J. Appl. Meteor. Climatol.*, **46**, 477–493, https://doi.org/10.1175/JAM2462.1.

Dee, D. P., and Coauthors, 2011: The ERA-Interim reanalysis: Configuration and performance of the data assimilation system. *Quart. J. Roy. Meteor. Soc.*, **137**, 553–597, https://doi.org/10.1002/qj.828.

Easterling, D. R., T. R. Karl, K. P. Gallo, D. A. Robinson, K. E. Trenberth, and A. Dai, 2000: Observed climate variability and change of relevance to the biosphere. *J. Geophys. Res.*, **105**, 20 101–20 114, https://doi.org/10.1029/2000JD900166.

Efstathiou, G. A., R. S. Plant, and M.-J. M. Bopape, 2018: Simulation of an evolving convective boundary layer using a scale-dependent dynamic Smagorinsky model at near-gray-zone resolutions. *J. Appl. Meteor. Climatol.*, **57**, 2197–2214, https://doi.org/10.1175/JAMC-D-17-0318.1.

Engelbrecht, C. J., and F. A. Engelbrecht, 2016: Shifts in Köppen–Geiger climate zones over southern Africa in relation to key global temperature goals. *Theor. Appl. Climatol.*, **123**, 247–261, https://doi.org/10.1007/s00704-014-1354-1.

Engelbrecht, F. A., J. L. McGregor, and C. J. D. Rautenbach, 2007: On the development of a new nonhydrostatic atmospheric model in South Africa. *S. Afr. J. Sci.*, **103**, 127–134.

——, ——, and C. J. Engelbrecht, 2009: Dynamics of the Conformal-Cubic Atmospheric Model projected climate-change signal over southern Africa. *Int. J. Climatol.*, **29**, 1013–1033, https://doi.org/10.1002/joc.1742.

——, W. A. Landman, C. J. Engelbrecht, S. Landman, M. M. Bopape, B. Roux, J. L. McGregor, and M. Thatcher, 2011: Multi-scale climate modeling over southern Africa using a variable-resolution global model. *Water S.A.*, **37**, 647–658, https://doi.org/10.4314/wsa.v37i5.2.

——, and Coauthors, 2015: Projections of rapidly rising surface temperatures over Africa under low mitigation. *Environ. Res. Lett.*, **10**, 085004, https://doi.org/10.1088/1748-9326/10/8/085004.

——, and Coauthors, 2019: Downscaling last glacial maximum climate over southern Africa. *Quat. Sci. Rev.*, **226**, 105879, https://doi.org/10.1016/j.quascirev.2019.105879.

Freidenreich, S. M., and V. Ramaswamy, 1999: A new multiple-band solar radiative parameterization for general circulation models. *J. Geophys. Res.*, **104**, 31 389–31 409, https://doi.org/10.1029/1999JD900456.

Garland, R. M., M. Matooane, F. A. Engelbrecht, M.-J. M. Bopape, W. A. Landman, M. Naidoo, J. Van der Merwe, and C. Y. Wright, 2015: Regional projections of extreme apparent temperature days in Africa and the related potential risk to human health. *Int. J. Environ. Res. Public Health*, **12**, 12 577–12 604, https://doi.org/10.3390/ijerph121012577.

Garuma, G. F., 2018: Review of urban surface parameterizations for numerical climate models. *Urban Climate*, **24**, 830–851, https://doi.org/10.1016/j.uclim.2017.10.006.

Gordon, N., and J. Shaykewich, 2000: On performance assessment of public weather services. WMO Tech. Doc. WMO/TD 1023, 67 pp., https://library.wmo.int/doc_num.php?explnum_id=5301.

Grimmond, C. S. B., and Coauthors, 2011: Initial results from phase 2 of the international urban energy balance model comparison. *Int. J. Climatol.*, **31**, 244–272, https://doi.org/10.1002/joc.2227.

Han, J.-Y., J.-J. Baik, and H. Lee, 2014: Urban impacts on precipitation. *Asia-Pac. J. Atmos. Sci.*, **50**, 17–30, https://doi.org/10.1007/s13143-014-0016-7.

Heaviside, C., H. Macintyre, and S. Vardoulakis, 2017: The urban heat island: Implications for health in a changing environment. *Curr. Environ. Health Rep.*, **4**, 296–305, https://doi.org/10.1007/s40572-017-0150-3.

Horowitz, H. M., R. M. Garland, M. Thatcher, W. A. Landman, Z. Dedekind, J. van der Merwe, and F. A. Engelbrecht, 2017: Evaluation of climate model aerosol seasonal and spatial variability over Africa using AERONET. *Atmos. Chem. Phys.*, **17**, 13 999–14 023, https://doi.org/10.5194/acp-17-13999-2017.

Hughes, W. S., and R. C. Balling Jr., 1996: Urban influences on South African temperature trends. *Int. J. Climatol.*, **16**, 935–940, https://doi.org/10.1002/(SICI)1097-0088(199608)16:8<935::AID-JOC64>3.0.CO;2-V.

Hurley, P., 2007: Modelling mean and turbulence fields in the dry convective boundary layer with the eddy-diffusivity/mass-flux approach. *Bound.-Layer Meteor.*, **125**, 525–536, https://doi.org/10.1007/s10546-007-9203-8.

Jones, P. D., C. Harpham, A. Troccoli, B. Gschwind, T. Ranchin, L. Wald, C. M. Goodess, and S. Dorling, 2017: Using ERA-Interim reanalysis for creating datasets of energy-relevant climate variables. *Earth Syst. Sci. Data*, **9**, 471–495, https://doi.org/10.5194/essd-9-471-2017.

Karl, T. R., and Coauthors, 1993: Asymmetric trends of daily maximum and minimum temperature. *Bull. Amer. Meteor. Soc.*, **74**, 1007–1024, https://doi.org/10.1175/1520-0477(1993)074<1007:ANPORG>2.0.CO;2.

Kottek, M., J. Grieser, C. Beck, B. Rudolf, and F. Rubel, 2006: World map of the Köppen–Geiger climate classification updated. *Meteor. Z.*, **15**, 259–263, https://doi.org/10.1127/0941-2948/2006/0130.

Kowalczyk, E. A., J. R. Garratt, and P. B. Krummel, 1994: Implementation of a soil-canopy scheme into the CSIRO GCM: Regional aspects of the model response. CSIRO Division of Atmospheric Research Tech. Paper 32, 65 pp., http://www.cmar.csiro.au/e-print/open/kowalczyk_1994a.pdf.

Kruger, A. C., and S. Shongwe, 2004: Temperature trends in South Africa: 1960–2003. *Int. J. Climatol.*, **24**, 1929–1945, https://doi.org/10.1002/joc.1096.

——, H. Rautenbach, S. Mbatha, S. Ngwenya, and T. E. Makgoale, 2019: Historical and projected trends in near-surface temperature indices for 22 locations in South Africa. *S. Afr. J. Sci.*, **115**, 1–9, https://doi.org/10.17159/sajs.2019/4846.

Lehoczky, A., J. Sobrino, D. Skoković, and E. Aguilar, 2017: The urban heat island effect in the city of Valencia: A case study for hot summer days. *Urban Sci.*, **1**, 9, https://doi.org/10.3390/urbansci1010009.

Lemonsu, A., C. Caillaud, A. Alias, S. Riette, Y. Seity, B. Le Roy, Y. Michau, and P. Lucas-Picher, 2023: What added value of CNRM-AROME convection-permitting regional climate model compared to CNRM-ALADIN regional climate model for urban climate studies? Evaluation over Paris area (France). *Climate Dyn.*, https://doi.org/10.1007/s00382-022-06647-w, in press.

Lipson, M. J., M. A. Hart, and M. Thatcher, 2017: Efficiently modelling urban heat storage: An interface conduction scheme in an urban land surface model (aTEB v2. 0). *Geosci. Model Dev.*, **10**, 991–1007, https://doi.org/10.5194/gmd-10-991-2017.

——, M. Thatcher, M. A. Hart, and A. Pitman, 2018: A building energy demand and urban land surface model. *Quart. J. Roy. Meteor. Soc.*, **144**, 1572–1590, https://doi.org/10.1002/qj.3317.

Luhar, A. K., M. Thatcher, and P. J. Hurley, 2014: Evaluating a building-averaged urban surface scheme in an operational mesoscale model for flow and dispersion. *Atmos. Environ.*, **88**, 47–58, https://doi.org/10.1016/j.atmosenv.2014.01.059.

Maisha, T. R., 2014: The influence of topography and model grid resolution on extreme weather forecasts over South-Africa. M.S. thesis, Faculty of Natural and Agricultural Science, University of Pretoria, 181 pp.

Masson, V., 2000: A physically-based scheme for the urban energy budget in atmospheric models. *Bound.-Layer Meteor.*, **94**, 357–397, https://doi.org/10.1023/A:1002463829265.

McGregor, J. L., 1996: Semi-Lagrangian advection on conformal-cubic grids. *Mon. Wea. Rev.*, **124**, 1311–1322, https://doi.org/10.1175/1520-0493(1996)124<1311:SLAOCC>2.0.CO;2.

——, K. C. Nguyen, and J. J. Katzfey, 2008: A variety of tropical climate simulations using CCAM. *High Resolution Modelling: Extended Abstracts of the Second CAWCR Modelling Workshop*, Melbourne, Australia, Bureau of Meteorology, 29–32.

Mirzaei, P. A., 2015: Recent challenges in modeling of urban heat island. *Sustainable Cities Soc.*, **19**, 200–206, https://doi.org/10.1016/j.scs.2015.04.001.

Muthige, M. S., J. Malherbe, F. A. Englebrecht, S. Grab, A. Beraki, T. R. Maisha, and J. van der Merwe, 2018: Projected changes in tropical cyclones over the south west Indian Ocean under different extents of global warming. *Environ. Res. Lett.*, **13**, 065019, https://doi.org/10.1088/1748-9326/aabc60.

Nguyen, K. C., J. J. Katzfey, and J. L. McGregor, 2014: Downscaling over Vietnam using the stretched-grid CCAM: Verification of the mean and interannual variability of rainfall. *Climate Dyn.*, **43**, 861–879, https://doi.org/10.1007/s00382-013-1976-5.

Nuruzzaman, M., 2015: Urban heat island: Causes, effects and mitigation measures – A review. *Int. J. Environ. Monit. Anal.*, **3**, 67–73, https://doi.org/10.11648/j.ijema.20150302.15.

Oleson, K. W., G. B. Bonan, J. Feddema, and T. Jackson, 2011: An examination of urban heat island characteristics in a global climate model. *Int. J. Climatol.*, **31**, 1848–1865, https://doi.org/10.1002/joc.2201.

Pokhrel, R., and H. Lee, 2011: Estimation of the effective zone of sea/land breeze in a coastal area. *Atmos. Pollut. Res.*, **2**, 106–115, https://doi.org/10.5094/APR.2011.013.

Ramamurthy, P., E. Bou-Zeid, J. A. Smith, Z. Wang, M. L. Baeck, N. Z. Saliendra, J. L. Hom, and C. Welty, 2014: Influence of subfacet heterogeneity and material properties on the urban surface energy budget. *J. Appl. Meteor. Climatol.*, **53**, 2114–2129, https://doi.org/10.1175/JAMC-D-13-0286.1.

Reichler, T., and J. Kim, 2008: How well do coupled models simulate today's climate? *Bull. Amer. Meteor. Soc.*, **89**, 303–312, https://doi.org/10.1175/BAMS-89-3-303.

Rotstayn, L. D., 1997: A physically based scheme for the treatment of stratiform clouds and precipitation in large-scale models. I: Description and evaluation of the microphysical processes. *Quart. J. Roy. Meteor. Soc.*, **123**, 1227–1282, https://doi.org/10.1002/qj.49712354106.

Sannigrahi, S., and Coauthors, 2018: Analyzing the role of biophysical compositions in minimizing urban land surface temperature and urban heating. *Urban Climate*, **24**, 803–819, https://doi.org/10.1016/j.uclim.2017.10.002.

Schleussner, C. F., and Coauthors, 2016: Differential climate impacts for policy-relevant limits to global warming: The case of 1.5°C and 2°C. *Earth Syst. Dyn.*, **7**, 327–351, https://doi.org/10.5194/esd-7-327-2016.

Sharma, A., P. Conry, H. J. S. Fernando, A. F. Hamlet, J. J. Hellmann, and F. Chen, 2016: Green and cool roofs to mitigate urban heat island effects in the Chicago metropolitan area: Evaluation with a regional climate model. *Environ. Res. Lett.*, **11**, 064004, https://doi.org/10.1088/1748-9326/11/6/064004.

Synnefa, A., M. Santamouris, and I. Livada, 2006: A study of the thermal performance of reflective coatings for the urban environment. *Sol. Energy*, **80**, 968–981, https://doi.org/10.1016/j.solener.2005.08.005.

Taha, H., 1997: Urban climates and heat islands: Albedo, evapotranspiration, and anthropogenic heat. *Energy Build.*, **25**, 99–103, https://doi.org/10.1016/S0378-7788(96)00999-1.

Thatcher, M., and J. L. McGregor, 2009: Using a scale-selective filter for dynamical downscaling with the conformal cubic atmospheric model. *Mon. Wea. Rev.*, **137**, 1742–1752, https://doi.org/10.1175/2008MWR2599.1.

——, and P. Hurley, 2012: Simulating Australian urban climate in a mesoscale atmospheric numerical model. *Bound.-Layer Meteor.*, **142**, 149–175, https://doi.org/10.1007/s10546-011-9663-8.

Thevakaran, A., J. L. McGregor, J. Katzfey, P. Hoffmann, R. Suppiah, and D. U. J. Sonnadara, 2016: An assessment of CSIRO conformal cubic atmospheric model simulations over Sri Lanka. *Climate Dyn.*, **46**, 1861–1875, https://doi.org/10.1007/s00382-015-2680-4.

Walsh, C. L., D. Roberts, R. J. Dawson, J. W. Hall, A. Nickson, and R. Hounsome, 2013: Experiences of integrated assessment of climate impacts, adaptation and mitigation modelling in London and Durban. *Environ. Urbanization*, **25**, 361–380, https://doi.org/10.1177/0956247813501121.

Wang, Z. H., and Q. Li, 2017: Thermodynamic characterisation of urban nocturnal cooling. *Heliyon*, **3**, e00290, https://doi.org/10.1016/j.heliyon.2017.e00290.

Wilby, R. L., 2008: Constructing climate change scenarios of urban heat island intensity and air quality. *Environ. Plann.*, **35B**, 902–919, https://doi.org/10.1068/b33066t.

Yan, G., D. Wen-Jie, R. Fu-Min, Z. Zong-Ci, and H. Jian-Bin, 2013: Surface air temperature simulations over China with CMIP5 and CMIP3. *Adv. Climate Chang. Res.*, **4**, 145–152, https://doi.org/10.3724/SP.J.1248.2013.145.

Yang, P., G. Ren, and W. Liu, 2013: Spatial and temporal characteristics of Beijing urban heat island intensity. *J. Appl. Meteor. Climatol.*, **52**, 1803–1816, https://doi.org/10.1175/JAMC-D-12-0125.1.

Zhang, J., L. Tian, and J. Lu, 2022: Temporal evolution of urban heat island and quantitative relationship with urbanization development in Chongqing, China. *Atmosphere*, **13**, 1594, https://doi.org/10.3390/atmos13101594.